OAK RIDGE
NATIONAL LABORATORY
MANAGED BY UT-BATTELLE
FOR THE DEPARTMENT OF ENERGY

ORNL/TM-2013/451

Final Report
Optimization Studies for ISOL-Type High-Powered Targets

November 2013

Prepared by
I. Remec
R. M. Ronningen

UT-BATTELLE
ORNL-27 (4-00)

ORNL/TM-2013/451

Reactor and Nuclear Systems Division

Final Report

Optimization Studies for ISOL-Type High-Powered Targets

I. Remec and R. M. Ronningen[*]

Date Published: November 2013

Prepared by
OAK RIDGE NATIONAL LABORATORY
Oak Ridge, Tennessee 37831-6283
managed by
UT-BATTELLE, LLC
for the
U.S. DEPARTMENT OF ENERGY
under contract DE-AC05-00OR22725

[*] Michigan State University

CONTENTS

Page

LIST OF FIGURES

LIST OF TABLES

EXECUTIVE SUMMARY

The research studied one-step (also known as direct) and two-step Isotope Separation on Line (ISOL) targets for future radioactive beam facilities with high driver-beam power through advanced computer simulations. Uranium carbide (UC_x) in the form of foils was used as a target material because of increasing demand for actinide targets in rare-isotope beam facilities and because such material was under development at the Isotope Separation and Acceleration Facility (ISAC) at TRIUMF when this project started. Simulations of effusion were performed for one-step and two-step targets, and the effects of target dimensions and foil matrix were studied. Diffusion simulations were limited by availability of diffusion parameters for UC_x material at reduced density; however, viability of the combined diffusion–effusion simulation methodology was demonstrated and could be used to extract physical parameters such as diffusion coefficients and effusion delay times from experimental isotope release curves. Dissipation of heat from the isotope-producing targets is the limiting factor for high-power beam operation both for the direct and two-step targets. Detailed target models were used to simulate proton beam interactions with the targets in order to obtain the fission rates and power deposition distributions, which were then applied in the heat transfer calculations to study the performance of the targets. Results indicate that a direct target, with specifications matching the ISAC TRIUMF target, could operate with a 500 MeV proton beam at beam powers up to ~40 kW, producing ~8×10^{13} fission/s, and with maximum temperature in UC_x not exceeding 2200°C. Targets with larger radii allow higher beam powers and fission rates. For a target radius in the range of 9 mm to 30 mm, the achievable fission rate increases almost linearly with target radius; however, the effusion delay time also increases linearly with target radius.

1. OVERVIEW OF EFFORTS

1.1 INTRODUCTION

This report is the final report for the project Optimization Studies for ISOL-Type High-Powered Targets. The project received $100K in funding, with $88K awarded to Oak Ridge National Laboratory (ORNL) (Grant number: ERKBE10) and $12K awarded to Michigan State University National Superconducting Cyclotron Laboratory (MSU-NSCL) (Grant number DE-FG02-07ER41474).

The title of the project was retained from the original proposal, which was for a three year effort funded at a $782K level; however, because of the reduced funding level, the scope of the project was reduced from optimization to exploratory parametric studies of the one- and two-step Isotope Separation on Line (ISOL) targets for future radioactive beam facilities with high driver-beam power through advanced computer simulations.

In this report, first a brief overview of the reasons driving this R&D effort will be given. Next, a short summary of our previous related work will be presented, followed by a detailed description of the research effort and results from this project.

1.2 BACKGROUND

Research with rare isotope ion beams has been recognized by both the nuclear and high-energy physics communities as one of the important fields of science. The scientific case for this interest can be summarized in the following questions. What is the origin of the elements in the cosmos, what are the limits of nuclear existence, what are the properties of nuclei with extreme ratios of neutrons to protons, what is the equation of state of neutron-rich nuclear matter, and is there physics beyond the standard model of particle physics?

At present, several rare isotope facilities in North America are operational at low and moderate beam power levels. Examples are **A**rgonne **T**andem **L**inear **A**ccelerator **S**ystem (ATLAS [1]), Michigan State University **N**ational **S**uperconducting **C**yclotron **L**aboratory (NSCL [2]), and Isotope Separator and Accelerator Facility (ISAC [3] at TRIUMF – Canada's national laboratory for particle and nuclear physics). The Holifield Radioactive Ion Beam Facility (HRIBF [4] at ORNL) ceased operations on April 15, 2012, after producing science for a half century.

Research at these facilities has been instrumental in identifying the scientific challenges, and this research can give answers to a number of questions. However, these facilities operate at limited powers, which in turn limit the achievable intensities of rare-isotope beams. ISAC, the current high-powered facility for isotope production in the North America, uses a driver beam of up to 50 kW of 500 MeV protons (100 μA). It has been recognized that substantial progress can only be made with a new generation of high-power facilities.

The US nuclear physics community's effort towards realizing a next-generation facility for rare isotope ion beams [5] has resulted in the design and establishment of the Facility for Rare Isotope Beams (FRIB) [6]. On August 1, 2013, the Department of Energy's Office of Science approved Critical Decision-2 (CD-2), Approve Performance Baseline, and Critical Decision-3a (CD-3a), Approve Start of Civil Construction and Long Lead Procurements, for the FRIB project, which will be located at Michigan State University.

FRIB is to be based on a driver linac capable of accelerating light and heavy ions with a beam power up to 400 kW and a specific energy of 200 MeV/nucleon for uranium. There are possibilities for energy

upgrades to ~1 GeV protons, ~500 MeV/nucleon for heavy ions such as xenon, and 400 MeV/nucleon for uranium.

1.3 PURPOSE

There are two main approaches for rare-isotope production: via projectile/target fragmentation reactions and via ISOL techniques.

The fragmentation approach uses heavy-ion beams impinging on targets consisting of lighter materials (e.g., carbon or lithium) – rare-isotopes are produced through fragmentation process, hence the name "fragmentation method' and "fragmentation targets." The beam of fragments is directed through a dipole magnet, which serves as a fragment separator, to the experimental stations. A relatively recently developed variation of the fragmentation method stops fast fragments in a stopping medium such as gas and reaccelerates them.

The ISOL method uses proton or light-ion beams impinging on high-Z targets (e.g., tungsten, mercury, uranium) to produce rare isotopes mainly through spallation and fission processes. Rare isotopes diffuse out of the ISOL target material and effuse to the ion source where they are ionized, accelerated, and sent through the dipole mass separator to the experimental stations.

The energy density and radiation damage rates in target systems for high-power facilities such as FRIB can be about five to eight times higher than those encountered at the ORNL Spallation Neutron Source (SNS) and TRIUMF ISAC targets; therefore, it is obvious that the challenges which will be encountered in the target design are substantial. To address these challenges was the main motivation and driver for the project we are reporting on here.

This project studies the ISOL targets. As a target material, we chose to use uranium carbide (UC_x) because of the increasing demand for actinide targets in rare-isotope beam facilities. ISOL targets were included in the early stages of the FRIB planning (when this project started) but are not incorporated in the current FRIB design; however, they would be a desirable addition at a later time, because every production method has specific advantages; more on this can be found in [7].

1.4 R&D COLLABORATION

The project was a collaborative effort carried out at the Oak Ridge National Laboratory (ORNL), the Michigan State University National Superconducting Cyclotron Laboratory (MSU-NSCL), and Scientific Investigation and Development (SID).

1.5 EXPERTISE IN COLLABORATION

The following radiation transport, rare isotope beam production, neutronics, heat transfer, and computational fluid dynamics experts at ORNL, MSU, and SID participated in this project:

- Inseok Baek, Georg Bollen, and Reg Ronningen, MSU-NSCL
- Ashraf Abdou, Ken Childs, Igor Remec, and Yan Zhang, ORNL
- Tony Gabriel, SID, 9608 Lyttleton Lane, Knoxville, TN 37922

1.6 FACILITIES AND RESOURCES USED IN THE R&D EFFORTS

ORNL has extensive analytical, computational, and experimental resources available to support this project. A wide range of computer codes, including MCNPX [8], PHITS [9], HEATING 7.2 [10], and ANSYS CFX5.7 [11] were used in this work. Several clusters of high-end PC's operating under LINUX with a distributed processing capability were available to the project.

MSU has extensive experience in accelerator design (cyclotrons, superconducting linear accelerator components), rare isotope production, and the design of fragment separators. MSU also has experience with several of the relevant computer codes (e.g., MCNPX, PHITS) and access to adequate computational resources to perform the work.

1.7 RELATED PROJECTS

This project is related to and draws from the following previously completed DOE-funded rare isotope accelerator (RIA) R&D and rare isotope beam (RIB) collaborative efforts and ORNL-funded projects:

- Development of a Concept for High Power Beam Dumps and Catchers, and the Pre-separator Area Layout for Fragment Separators for the Rare Isotope Accelerator Project (funded under DE-FG02-04ER41313);
- Development of a Concept for the ISOL Target Areas for RIA (funded under DE-FG02-04ER41322);
- Determination of Component Activation and Radiation Environment in the RIA Second Stripper Region (funded under DE-FG02-05ER41403);
- Studies of Limits on Uncontrolled Heavy Ion Beam Losses for Allowing Hands-On Maintenance (funded under DE-FG02-07ER41475); and
- Optimization Studies for ISOL-Type High-Powered Targets [funded as an ORNL Laboratory Directed Research and Development (LDRD) project].

1.8 PROJECT PUBLICATIONS

In addition to the present report, the results of this project were published in the following publications:

Y. Zhang, I. Remec, G. D. Alton, and Z. Liu, "Simulation of Rare Isotope Release from ISOL Target," *Nucl. Instru. Meth. Phys. Res. A*, Vol. 620 (2010) 142 (available online at http://dx.doi.org/10.1016/j.nima.2010.04.015).

Y. Zhang, I. Remec, and Z. Liu, "ISOL Target–Vapor Transport System Simulations," Proceedings of the 23rd Particle Accelerator Conference (PAC09) 4–8May 2009, Vancouver, British Columbia, Canada, p 2850 (available online at http://accelconf.web.cern.ch/AccelConf/PAC2009/papers/we6rfp028.pdf).

2. RESEARCH EFFORT AND RESULTS

In the next two sections, we summarize our previous work on one-step and two-step targets. In the following chapters, we discuss details of the present research effort and results of this project.

2.1 PREVIOUS WORK ON ONE-STEP TARGETS

Our initial investigations of the one-step (direct) target were performed with a simplified model (Figure 1), which consisted of a cylindrical tantalum can 100 mm long with an inner radius of 10 mm and walls 2 mm thick [12]. The inside was completely filled with UC at 6 g cm^{-3}; low UC density was used to reflect porous material or homogenization of foils and voids between them. A 5 mm thick radial gap separated the target from the cooling structure, which was modeled as two concentric stainless steel tubes with a 4 mm water-filled layer. The cooling structure is not important for the studies of the beam interactions with the target and is included here just to provide a complete description of the model used in the simulations.

Simulations of driver-beam interaction with the target were performed with the MCNPX [8] and PHITS [9] codes, and good agreement (within a few %) was observed for all the parameters of interest, such as number of neutrons generated and energy deposition per proton in the target.

For the driver beam, three candidates were considered: 1 GeV protons, 1.244 GeV deuterons, and 2.331 GeV He-3 ions. The results are summarized in Table 1; statistical uncertainties were typically small (less than 1%) and are not reported here.

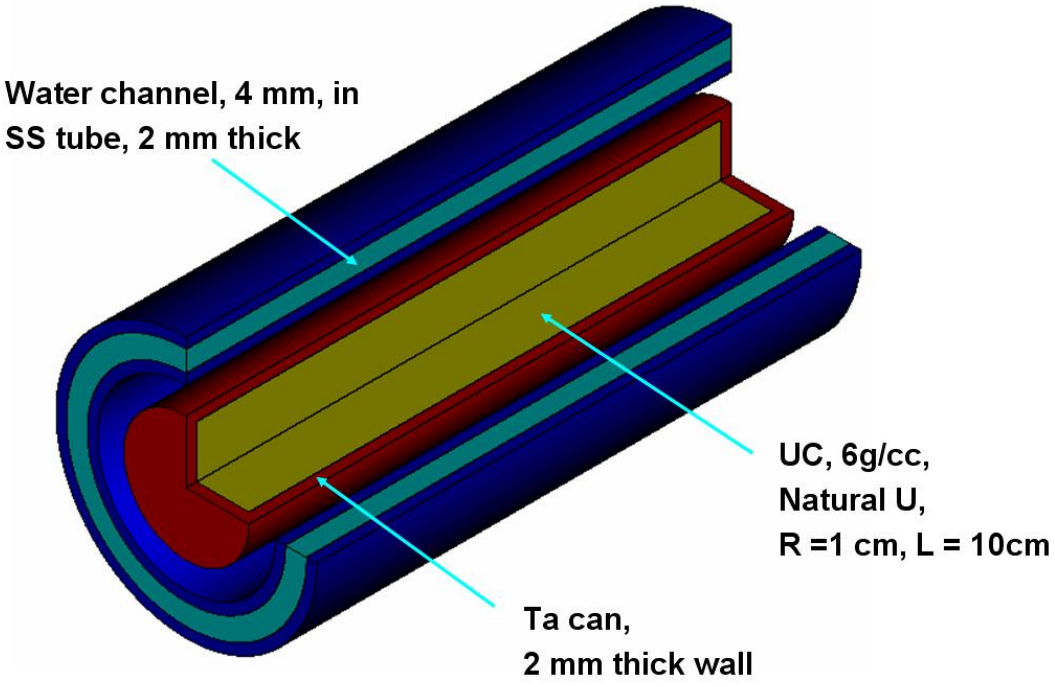

Figure 1. Simplified one-step target model used for the simulations of driver-beam interaction with the target.

Table 1. Comparison of fission rates and energy deposited in UC for different primary beams at the beam power of 400 kW; direct target, 1 cm radius, 10 cm long, UC at 6 g cm^{-3}

Beam	Fission rate		Energy deposited in UC	
	s^{-1}	Relative to proton beam	kW	Relative to proton beam
p, 1-GeV	5.90E+14	1.00	50	1.00
d, 1.244-GeV	3.09E+14	0.52	43	0.86
He-3, 2.331-GeV	2.22E+14	0.38	60	1.21

The fission rates given in Table 1 are normalized to the beam power of 400 kW, since this was the projected power for the FRIB facility; for the moment, we disregard the fact that such a high power beam would result in target temperatures above the maximum allowable temperature, as discussed later. It is important to compare the driver beams at equal beam power, because the particle current of 1 GeV protons is higher than the particle current of 1.244 GeV deuterons, which is 80% of the proton current, and the 2.331 GeV He-3 particle current is only 43% of the proton current.

The 1 GeV proton beam provides the most favorable results; it produces almost twice the fission events of the 1.244 GeV deuteron beam, and almost three times more fissions than the 2.331 GeV He-3 beam. At 400 kW beam power, the target heating rate (total energy deposited in the target) is 50 kW for the 1 GeV proton beam; the heating rate is ~14% lower for the 1.244 GeV deuteron beam and ~20% higher for the 2.331 GeV He-3 beam.

As anticipated, high heating rates in the target were observed and proved to be the limiting factor for the beam power if the temperature of the UC is to be kept below ~2200°C. For the 1 GeV proton beam, the 50 kW energy deposition in the UC results in an average power density of ~1.6 MW per liter, which is about five times higher than the average power density in the fuel of a typical commercial pressurized water nuclear reactor.

With the energy deposition rate obtained from the transport calculations for a 1 GeV proton beam, a thermal analysis of the target was carried out with the HEATING7 code [10], a multidimensional, finite-difference code system for heat transfer analysis. The experimental temperature-dependent thermal conductivity data for UC_2 are shown in Figure 2; specifically the values for the Sample 3 were used in our analyses [13]. Sample 3 data (with relatively high thermal conductivity) were selected because the ongoing efforts were expected to produce UC_2 targets with similar or higher thermal conductivity. The target was cooled by the thermal radiation from the outer radial surface to an adjacent cooled surface, which was assumed to be at 200°C. There was a 10 mm gap between the outer surface and adjacent cooled surface. The beam power was reduced, so that the maximum temperature in the UC was below 2200°C. For an emissivity of 0.5, the allowable beam power was found to be 19 kW, which produces 2.80×10^{13} fission/s in the target. For the black body surface (emissivity 1.00), the beam power was ~46 kW, and the fission rate was 6.79×10^{13} fission/s. The allowable beam power therefore highly depended on the emissivity of the container.

Estimates of the effects of the target radius and the thermal conductivity of UC were also performed, albeit in an approximate way. The thermal conductivity of UC was assumed to be constant (not temperature dependent); the front and back surfaces of the target were assumed adiabatic; and the heat was conducted through UC in the radial direction only and was dissipated from the surface by thermal radiation. The energy deposition and conduction through the target container was not taken into account. Thermal conductivity of UC was found to be quite important; an increase in the thermal conductivity from 5 W/m/K to 15 W/m/K allowed an increase of the beam power of ~50% for a 1 cm radius target, and 100% for a target with a 5 cm radius. On the other hand, increasing the target radius was not effective for increasing beam power; changing the target radius from 1 cm to 5 cm allowed only about 50% higher

maximum beam power; however, the volume and mass of UC in the target were 25 times greater (UC thermal conductivity was assumed to be 10 W/m/K and emissivity was 0.5).

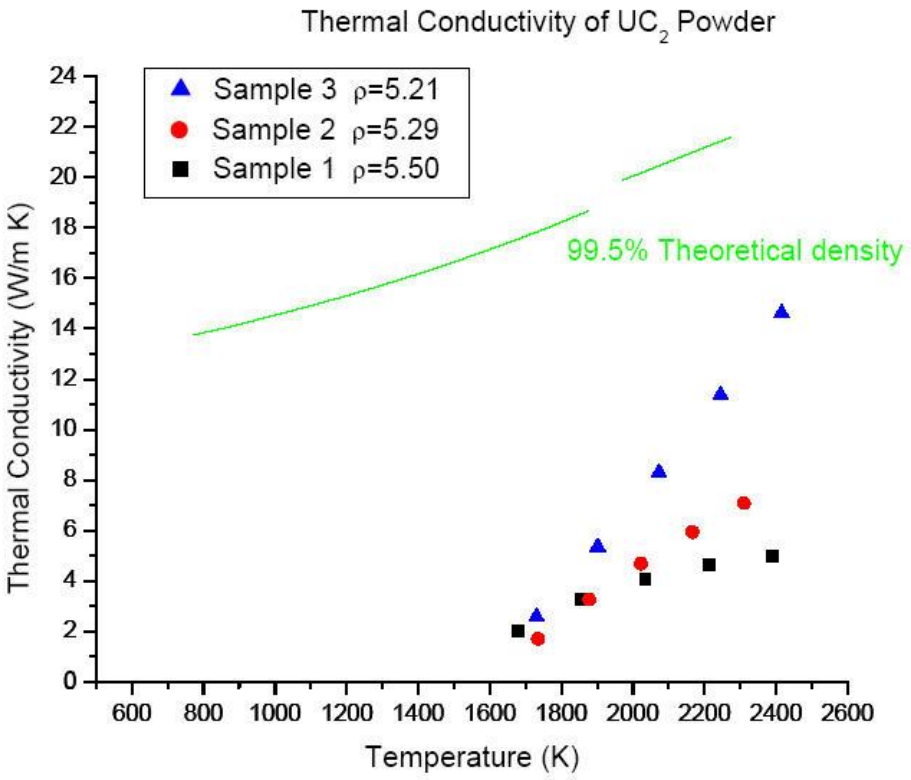

Figure 2. Thermal conductivity of UC_2 samples at reduced density [13].

2.2 PREVIOUS WORK ON TWO-STEP TARGETS

In the two-step target concept, the energetic primary "driver" beam generates neutrons in the primary target. The neutrons subsequently produce rare isotopes through fissions in the secondary target. The driver beam interacts with the primary target only. The large energy deposition due to slowing down of the primary beam is confined to the primary target. The heat load of the secondary target is reduced, which is desirable. Because the spallation reactions occur in the primary target, which is separated from the secondary target where the rare isotopes are produced, the isobar contamination in the production of the neutron-rich fission products should be reduced.

In our previous investigations of the effects of the different driver-beams, a simplified two-step target model shown in Figure 3 was used [12]. The model included only the basic components deemed to be important for the study; the engineering details needed for realization of such a target were not considered. The primary target has a radius of 1.27 cm and is 15 cm long. The walls of the primary target stainless steel container are 3 mm thick. A 7 mm thick radial gap separates the primary and secondary targets. The secondary target consists of a 45 cm long hollow cylinder with a 5 cm radial thickness of UC_x, housed in a 3 mm thick tantalum container. For the primary target material, mercury and tungsten cooled with water (with water volumes 10% and 20% of the primary target) were considered.

Simulations of driver-beam interaction with the target were performed with the MCNPX and PHITS codes. As for the one-step targets, the 1 GeV proton, 1.244 GeV deuteron, and 2.331 GeV He-3 driver

beams were considered. Table 2, 3, and 4 summarize comparisons of the number of fissions induced in the secondary target, energy deposited in the secondary target, and energy deposited in the primary target; statistical uncertainties of the results were typically small (less than 1%) and are not reported here.

The 1 GeV proton and 1.244 GeV deuteron beams are largely equivalent; they produce about the same number of fissions in the secondary target and about an equal amount of heating in the primary and secondary targets. This finding is remarkably different from the one-step targets, where the proton beam delivered, by far, the best performance. The 2.331 GeV He-3 beam is clearly less favorable: it gives ~15% less fissions in the secondary target and much higher heating load in the primary target, 45% higher for the mercury primary target, and even 72% higher for the water-cooled-tungsten primary target.

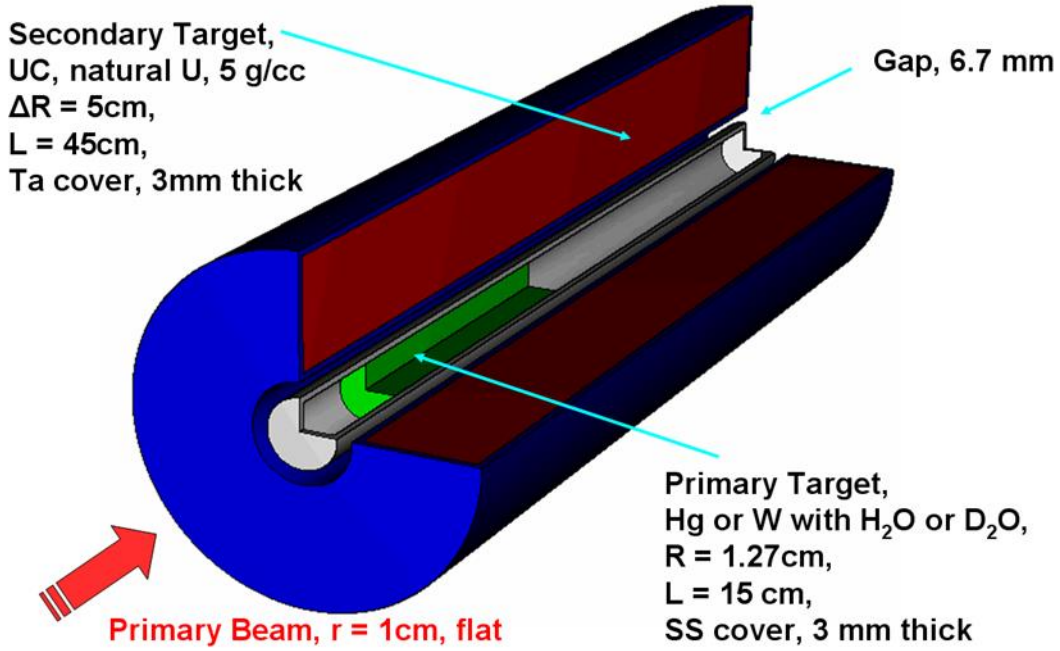

Figure 3. Simplified two-step target model used for the simulations of driver-beam interaction with the target.

The primary targets of mercury and water-cooled tungsten performed almost identically with respect to the fission rate and energy deposition in the secondary target; however, the heat load of the primary target was ~20–30% higher for the water-cooled tungsten. The cladding necessary to prevent water-induced corrosion of tungsten was not included in the models. Replacing water with heavy water showed no effect on performance.

Table 2. Number of fissions in the secondary target, for the p, d, and He-3 beam, at 400 kW beam power (ratios to the p beam on mercury target are given for other beams and targets)

Driver beam, energy	Number of fissions in the secondary target	
	Primary target composition	
	Hg	0.9 W + 0.1 H_2O[a]
p, 1 GeV	1.8×10^{15} fissions/s	1.03 (1.00)[b]
d, 1.244 GeV	0.99	1.05
He-3, 2.331 GeV	0.85	0.86

[a]The target is a homogeneous mixture of 90% tungsten and 10% water by volume.
[b]In parentheses are the values for the primary target with 80% tungsten and 20% water by volume.

Table 3. Energy deposited in the secondary target (including fission energy) for the p, d, and He-3 beam, at 400 kW beam power (ratios to the p beam on mercury target are given for other beams and targets)

Driver beam, energy	Energy deposited in the secondary target	
	Primary target composition	
	Hg	0.9 W + 0.1 H_2O[a]
p, 1 GeV	84 kW	1.02 (1.01)[b]
d, 1.244 GeV	0.96	1.01
He-3, 2.331 GeV	0.87	0.85

[a]The target is a homogeneous mixture of 90% tungsten and 10% water by volume.
[b]In parentheses are the values for the primary target with 80% tungsten and 20% water by volume.

Table 4. Energy deposited in the primary target for the p, d, and He-3 beam, at 400 kW beam power (ratios to the p beam on mercury target are given for other beams and targets)

Driver beam, energy	Energy deposited in the primary target	
	Primary target composition	
	Hg	0.9 W + 0.1 H_2O[a]
p, 1 GeV	106 kW	1.19 (1.32)[b]
d, 1.244 GeV	0.99	1.20
He-3, 2.331 GeV	1.44	1.72

[a]The target is a homogeneous mixture of 90% tungsten and 10% water by volume.
[b]In parentheses are the values for the primary target with 80% tungsten and 20% water by volume.

The feasibility of cooling the tungsten primary target with water was investigated with computational fluid dynamics (CFD) simulations performed with the ANSYS code. It was determined that for the maximum heating rate of ~5 kW cm^{-3} — which is higher than the maximum heating rate for a 1 GeV proton beam and a 1.244 GeV deuteron beam at 400 kW but slightly lower than the maximum for a 2.331 GeV He-3 beam — cooling can be accomplished with water flow, and the required volume of the water channels would be ~20% of the primary target. Therefore, cooling of the primary target does not appear to be a limiting factor for the operation of two-step targets.

Even with the primary beam energy deposition being mostly limited to the primary target, cooling of the secondary target remains the limiting factor for target operation. For the 1 GeV proton beam at 400 kW, the energy deposition in the secondary target was 84 kW. Fissions account for ~58 kW, and scattered primary beam and secondary particles reaching the secondary target contribute the remaining 26 kW.

The heat transfer calculations for the secondary targets were carried out with the HEATING7 code with energy deposition distributions obtained from the simulations with the PHITS or MCNPX codes. In the heat transfer calculations, it was assumed that heat was dissipated by thermal radiation from the secondary target to cooled surfaces adjacent to both the inner and outer radii of the secondary target. The gap between the inner radius of the secondary target and the inner cooled surface was 7 mm. The gap between the outer radius of the secondary target and the outer cooled surface was 10 mm. The front and back outer surfaces of the target were assumed adiabatic; all other surfaces were assumed to behave as gray bodies with an emissivity of 0.5. Both cooled surfaces (which were not part of the secondary target) were assumed to be at a constant temperature of 200°C.

To produce intense beams of rare isotopes, it is desirable, among other factors, to maximize the number of fissions in the secondary target, maintain target material at high temperature but lower than 2200°C for UC_x, and maintain a uniform temperature distribution in the target. With these objectives and starting from the initial model shown in Figure 3, the target was systematically modified and reanalyzed. Parameters considered were length and thickness of the secondary target, UC_2 density (uniform in the target), variable UC_2 density in the radial direction, as well as in the axial direction, length, and position of the primary target.

An example of the results is given in Figure 4, which depicts energy deposited in the secondary target, and primary beam power, versus the thickness of the UC_2 in the secondary target. The beam power was adjusted to obtain the maximum temperature of 2200°C in the UC_x. The analysis was performed for secondary target radial thicknesses of 2, 3, 4, and 5 cm. A change in thickness from 2 cm to 5 cm resulted in practically no increase in power which can be deposited in the secondary target –the allowable power increased only from 23.2 kW to 23.7 kW, because the increased size adversely affected heat transfer. However, a 5 cm thick secondary target can reach about the same energy deposition (and fission rate) as the 2 cm thick target with only about 50% of the beam power required for the 2 cm thick target.

In the analysis depicted in Figure 4, the heat transfer calculations modeled the UC_2 as 100 discs separated with small gaps. A small radial gap was also assumed between the outer boundary of the UC_2 discs and the inner boundary of the tantalum can. The thermal conductivity of the UC_2 was assumed to be equal to sample 3 in Figure 2.

The best secondary target configuration achieved with the analysis described above is shown in Figure 5. The length of the target is 25 cm, and the radial thickness is 4 cm. The primary target (not shown) is 15 cm long, has a radius of 1.27 cm, and is in a 3 mm thick steel container. The middle section consists of UC_2/C_{gr} composite material, while the left and right segments are filled with UC_2 at the density of 5.21 g cm^{-3}(which is the density of the sample 3 in Figure 2). The UC_2/C_{gr} is a special composite foil material, consisting of a flexible exfoliated graphite sheet core with thin sintered UC_2 layers on one side. This material was developed at TRIUMF as a special target material [14] when these studies were performed. The composite foils have higher conductivity than UC_2 and allow higher heating rate in the secondary target. For the two parts of the outer surface of the target, one at the front (left) end and the second at the back end, which are marked with blue lines on Figure 5, adiabatic boundary conditions were used. This resulted in a much more uniform temperature distribution in the target. For this target, the fission rate is 3.74 E+14 fission/s, at the proton beam power 143 kW and the secondary target heating 27.3 kW.

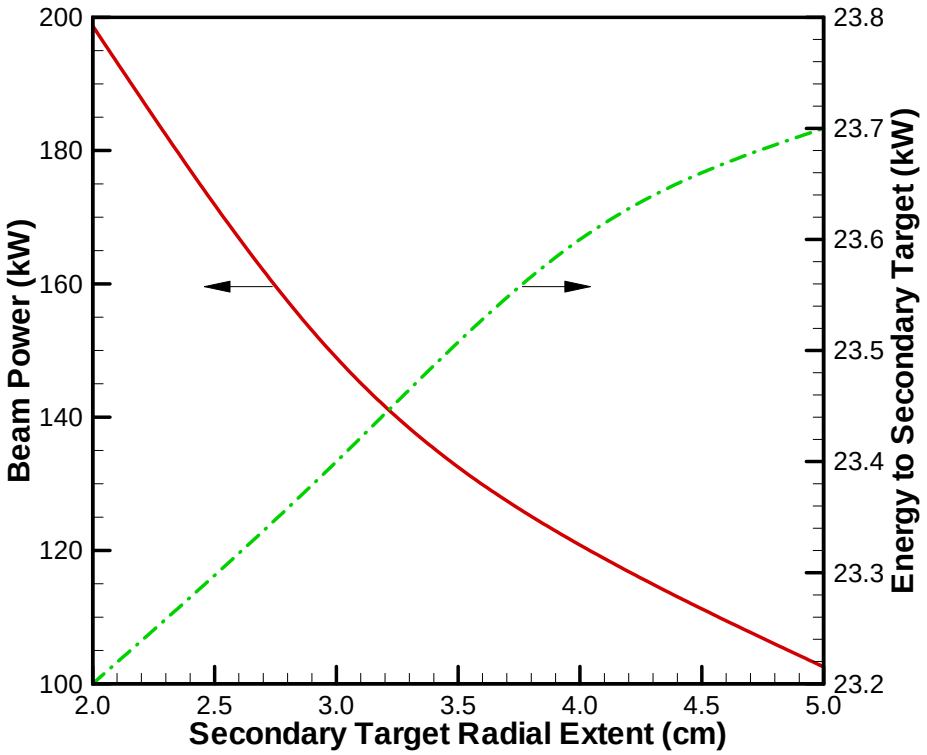

Figure 4. Energy deposited in the secondary target (green line) and primary beam power (red line) versus the thickness of the UC_2 in the secondary target. The beam power was adjusted to obtain the maximum temperature of 2200°C.

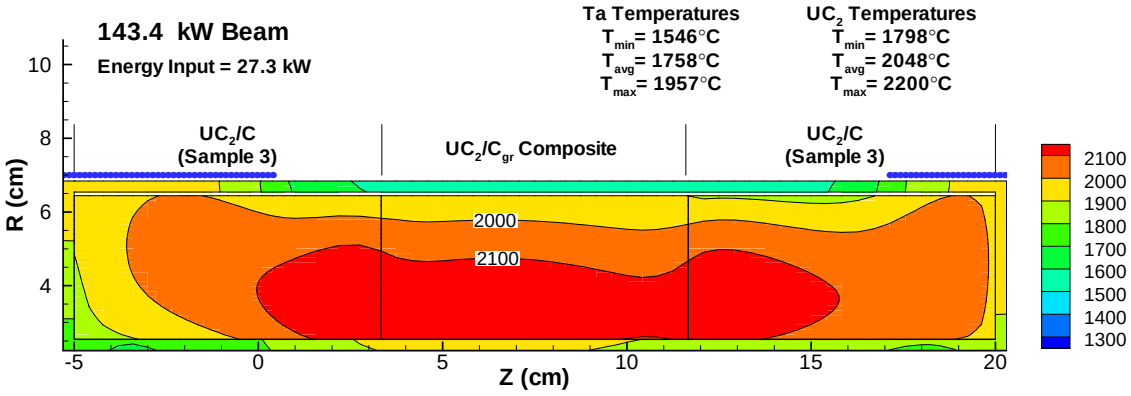

Figure 5. Selected best case of the secondary target configuration. The middle section consists of UC_2/C_{gr} composite material, while the left and right segments are filled with UC_2 at the density of 5.21 g cm^{-3}.

To improve the cooling of the secondary target, active cooling can be added; however, this significantly increases the complexity of the target design. An example of such a target is shown in Figure 6. Due to the symmetry, only a 30 degree segment of the model is shown. Six channels extend inside the secondary target volume from the target inner surface. Coolant flow enters the channels at the middle of the target

length, splits, and flows axially towards both ends of the target. The radial thickness of UC_2 was again 4 cm, the density was 5 g cm^{-3}, and the thermal conductivity of sample 3 in Figure 2 was assumed.

When helium is used as a coolant, the maximum temperature in the UC_2 of 2200°C is reached for secondary target heating of 37 kW, fission rate of 5.4 E+14 fissions/s, and proton beam power of 202 kW. This represents ~40% improvement in the number of fissions over the case without active cooling of the secondary target.

When sodium is used as a coolant, the maximum temperature of UC_2 at 2200°C is reached at secondary target heating of 54 kW, fission rate 7.7 E+14 fission/s, and primary beam power of 290 kW. Using sodium as a coolant results in a large increase, ~40%, in the obtainable fission rate with respect to the helium coolant, and it doubles the fission rate with respect to the secondary target without active cooling; however, it adds all of the complexities of dealing with sodium.

Adding active cooling to the secondary target therefore allows an increase in the achievable fission rate in the range from 50% to a factor of 2.

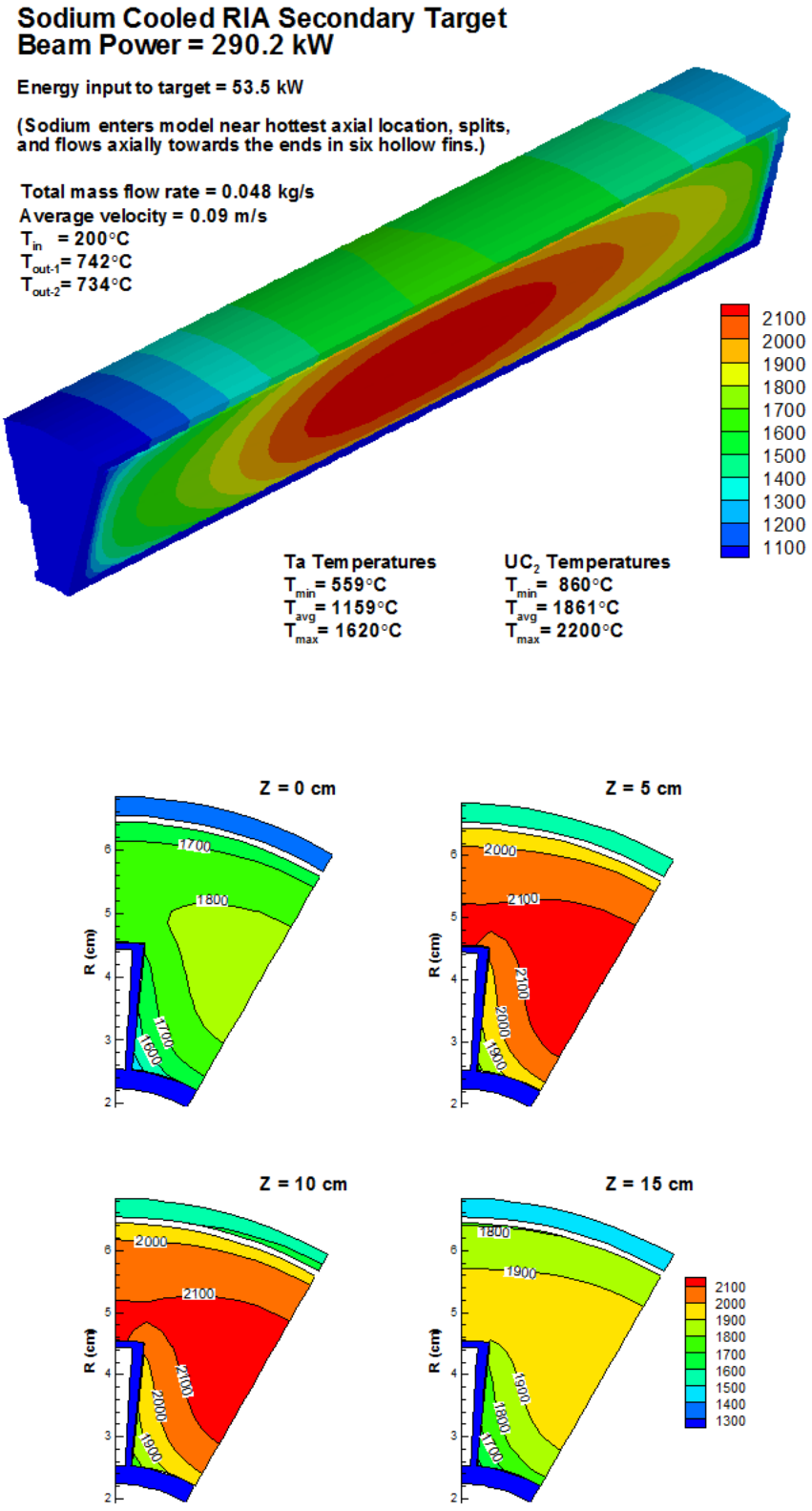

Figure 6. Secondary target with active cooling. There are six cooling channels extending into the target from the inner surface. Results for sodium coolant are shown.

2.3 EFFUSION AND DIFFUSION SIMULATIONS

Rare isotopes diffuse out of ISOL target material and effuse to the ion source where they are ionized, accelerated, and sent through the dipole mass separator to the experimental stations. For radioactive short-lived isotopes, decay during diffusion and effusion significantly reduces the intensity of the beams of isotopes available for the experiments. In the following sections, an attempt is made to gain insight in some parameters affecting diffusion and effusion processes in ISOL targets through simulations.

2.3.1 Effusion Simulations Approach

Work on the Optimization Studies for ISOL-Type High-Powered Targets project started with effusion and diffusion simulations, because this aspect was not covered in our previous work, which was centered on investigating driver-beam interactions with targets, achievable fission rates, and temperature and cooling issues.

In the vacuum conditions in rare-isotope-producing targets, the isotope mean free path is typically much longer than the characteristic dimension of the target system; in other words, the molecular-flow (Knudsen) condition exists. The kinetic theory of gasses can be used to derive a general expression giving the number of particles N left in an arbitrary size and geometry system after an evacuation time t:

$$N(t) = N_0 \times e^{-\frac{t}{t_C}}, \quad (1)$$

where N_0 is the number of particles in the system at $t = 0$, and t_c is the average time the particle stays in the system.

The characteristic evacuation time for a tube with one end closed is [15]

$$t_C = \frac{4V}{\pi^2 C}, \quad (2)$$

where V is the volume and C is the conductance of the straight tube with both ends open.

For systems with different geometry and chemically active particles that interact with the walls, the average distance traveled by a particle in the transport system can be described by a more generalized formula [16]:

$$t_C = N_b \tau_0 \cdot e^{\frac{H_{ad}}{k \cdot T}} + \frac{l}{1.397 \times v}, \quad (3)$$

where H_{ad} is the enthalpy of adsorption for the particle on a given surface; N_b is the characteristic number of surface collisions with the walls of the target system during transport; l is the average distance traveled by a particle in the transport system; v is the average velocity of Maxwell-Boltzmann velocity distribution; T is the absolute temperature; k is the Boltzmann constant; and τ_0 is a time constant ($\tau_0 \approx 3.4 \times 10^{-15}$ s). The first term in Eq. (3) depends on the interaction of specific effusing particles with target surfaces. It is typically negligible for non-reactive atoms and molecules such as noble elements. However, for all reactive particles it is proportional to the average number of collisions that a particle experiences while travelling through the target; therefore, more collisions correspond to longer t_c. The second term in Eq. (3) is proportional to the average length of the trajectory that the particle travels in the target. Therefore, in general, non-particle-specific evaluation of the targets, from the effusion point of view, can simply rely on these two parameters; fewer collisions and shorter average trajectory length imply a better target.

For systems with complicated geometries, simple estimates of t_c are not possible, and applications of vacuum conductance theory are not accurate enough. However, Monte Carlo techniques can produce very accurate solutions even for complicated systems.

An ORNL computer code "Effusion" was developed to simulate effusive-flow of neutral particles through complicated vacuum systems [17]. Effusion is based on the GEANT toolkit [18]. GEANT4 is a particle detector simulation toolkit that fully supports three-dimensional geometries and particle tracking. In the Effusion code, the average distance traveled per particle is assumed to be completely independent of target material and the system operational temperature. Particle-particle collisions are ignored. A typical Effusion simulation tracks 10,000 particles through a target to determine the average path length. The results are sensitive to the modeling of the angular distribution of particles reemitted from surfaces following adsorption. In the Effusion code, three options are available: isotropic distribution about the surface normal, cosine distribution about the surface normal, and specular reflection. Simulations with these three different options showed that isotropic particle reemission is the most adequate: it produced excellent agreement of simulation results with theoretical predictions for simple cases and with experimental results [17]. The Effusion code was extensively used to simulate two-step and one-step targets. For the Optimization project, a parallel version of the Effusion code was developed. This made possible the simulations of two-step targets, which required considerable computer time. Results will be discussed in the following sections.

2.3.2 Effusion Simulations Results for Two-Step Targets

First we performed a series of simulations of the effusion flow through the secondary (production) target of the two-step ISOL target. We considered a cylindrical target, 25 cm long, with inner radius of 5 cm and outer radius of 15 cm. The target volume was filled with UC_2 disks separated by empty channels to facilitate the effusion flow. There was an annular (radial) gap between the edge of the disks and the cylindrical container (Figure 7) intended to facilitate the effusion from the target to the extraction pipe. Each disk in Figure 7 was 2.14 mm thick, and 30 UC_2 disks were placed in the container, spaced 6 mm apart (ΔZ). The annular gap between the container and the disks was 10 mm (ΔR). Figures 7 and 8 show a trajectory of a single particle. A dramatic difference is readily observed: for largely spaced UC_2 disks (6 mm disk-to-disk gap) and a large annular gap between the disks and container (10 mm), the particle trajectory appears to be uniformly spread through the target (Figure 7). For the tightly spaced disks (~ 0.1 mm apart) and small annular gap (2 mm), only a few segments of the trajectory reach the space between the disks and the particle travels mostly within the annular gap to the exit. For the disks packed tightly, so that the disk thickness is much larger than the gap between the disks, one would intuitively expect that once the particle reaches the annular gap, the probability that the particle reenters the space between the disks is small. The simulation therefore readily confirms intuitive expectations.

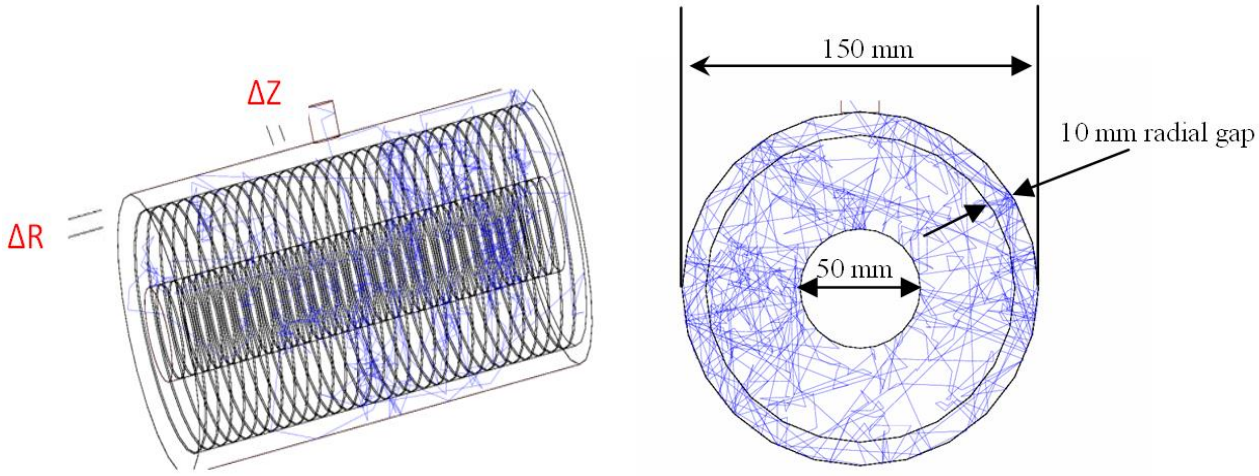

Figure 7. A trajectory of a single particle effusing from the two-step ISOL target. The particle track is shown in blue. On the left side a three-dimensional sketch is shown, and on the right the projection of the trajectories on the plane perpendicular to the target axis is displayed.

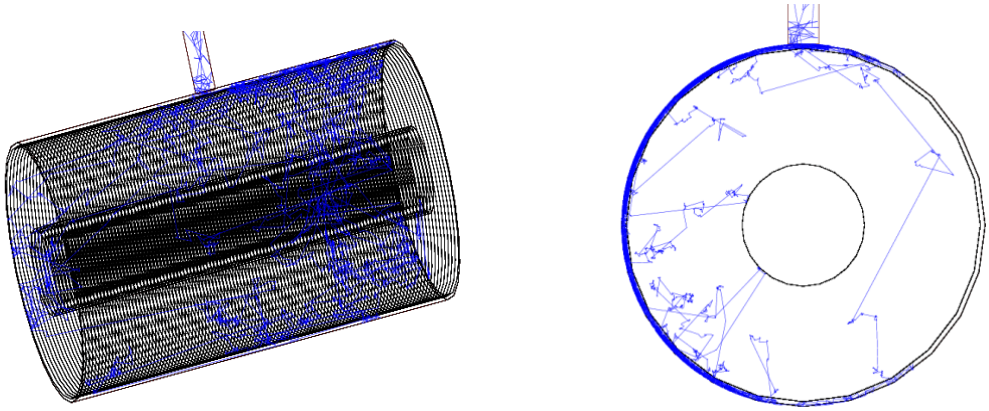

Figure 8. As Fig. 7, but there are 113 disks in the container, spaced less than 0.1 mm apart, and the annular gap is 2 mm wide.

To investigate the effect of disk spacing (ΔZ) and annular gap thickness (ΔR), a series of simulations was performed. A 25 cm long target with a 5 cm inner diameter and a 15 cm outer diameter, filled with 4.3 mm thick disks, was considered. Figure 9 depicts the average length of the particle track inside the target versus matrix spacing, and Figure 10 shows the average number of particle collisions with surfaces in the target versus matrix spacing. Numerical values obtained from simulations are listed in Tables 5 and 6.

For all disk spacings, the average distance travelled reaches a minimum at an annular gap thickness in the range of 1 mm to 2 mm. The minimum is more pronounced for smaller ΔZ. For ΔR smaller than ~ 1 mm, the average track length increases rapidly. The average number of collisions with surfaces decreases with increasing ΔR; however, the effect is pronounced only for ΔR smaller than ~ 1 mm. Hence, it appears that the ΔR in the range of 1 mm to 2 mm is preferred.

The average track length decreases when disk spacing decreases, for all ΔR. However, the number of collisions with surfaces increases with decreasing ΔZ, for all ΔR. The increase is quite pronounced for ΔR smaller than ~1 mm and much less important for larger ΔR. Since disk spacing has the opposite effect on track length and number of collisions, this indicates that specific target tuning may be possible for the target-particle combinations which display surface sticking times long enough that the first term in Eq. (3) becomes significant. For ΔR = 2 mm, decreasing ΔZ from 1.5 mm to 0.1mm increases the number of collisions 1.5 times and shortens the average path length by approximately three times. Thus, even in the case that the two terms in Eq. (3) are comparable, smaller disk spacing results in shorter evacuation times.

Therefore a combination of annular gap of ~2 mm and disk spacing of ~0.1 mm appears to be recommended.

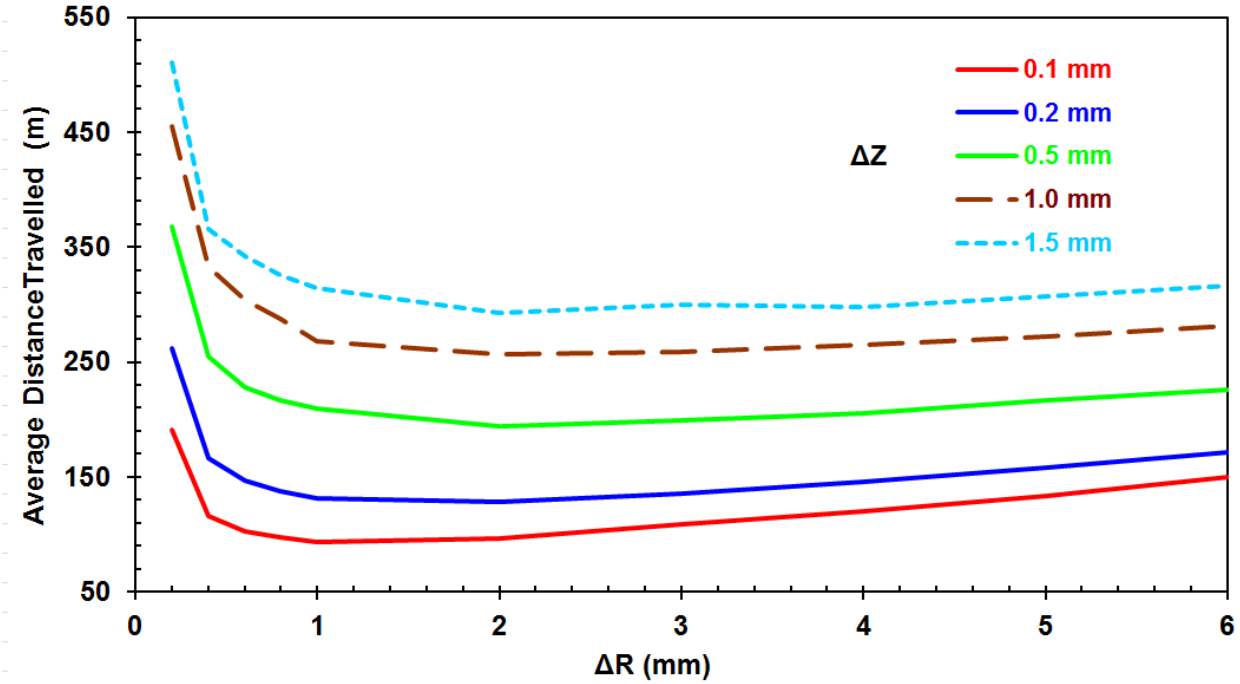

Figure 9. The average length of particle track versus disk spacing and annular gap thickness.

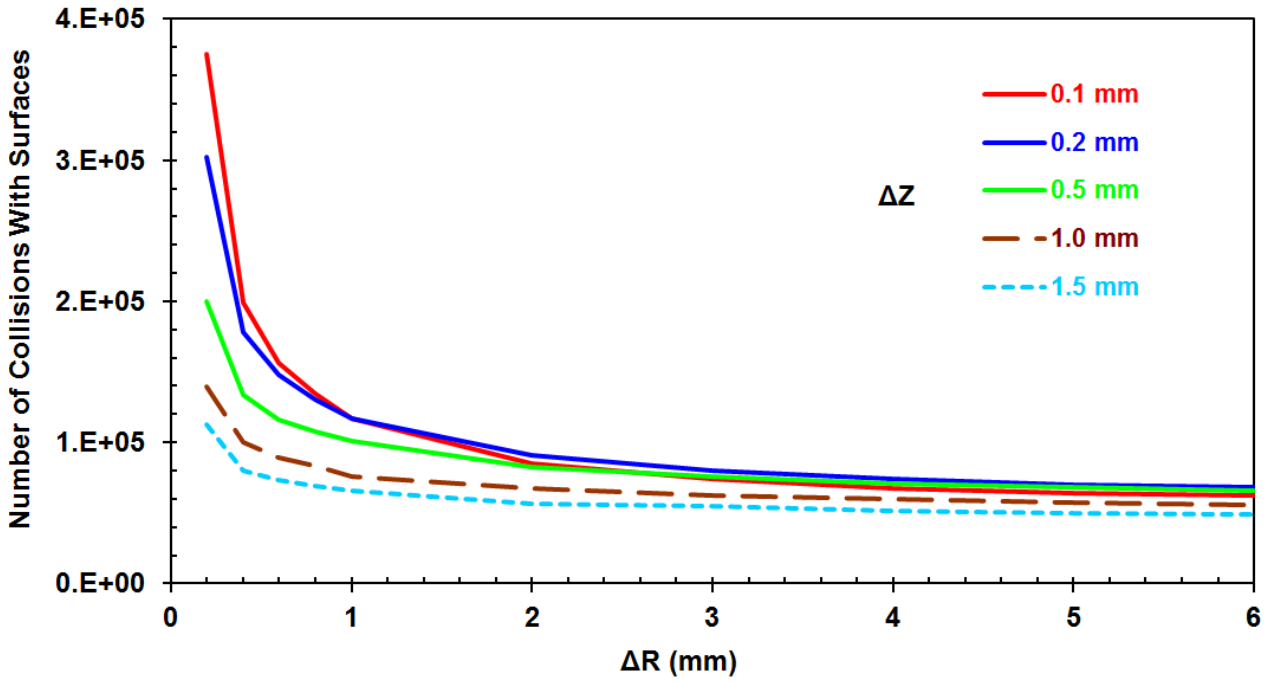

Figure 10. The average number of particle collisions with surfaces versus disk spacing and annular gap thickness.

Table 5. Average particle track length in meters versus disk spacing (ΔZ) and the thickness of annular gap (ΔR)

	ΔZ [mm]				
ΔR [mm]	**0.1**	**0.2**	**0.5**	**1.0**	**1.5**
0.2	190	262	368	455	510
0.4	116	166	255	333	366
0.6	103	147	228	304	342
0.8	97.9	137	217	287	326
1	93.5	131	209	268	314
2	96.5	129	194	256	293
3	108	135	200	259	300
4	120	146	206	265	297
5	134	158	216	272	307
6	150	172	226	281	316

Table 6. Average number of collisions with surfaces versus disk spacing (ΔZ) and the thickness of annular gap (ΔR)

	ΔZ [mm]				
ΔR [mm]	**0.1**	**0.2**	**0.5**	**1.0**	**1.5**
0.2	375519	302560	200135	139888	113101
0.4	199052	178396	134018	100272	79777
0.6	156513	147905	116120	89576	73336
0.8	134133	129933	107540	83217	68850
1	116910	117201	100673	76210	65403
2	84893	91071	82347	67034	56899
3	74190	79672	75742	62743	54829
4	67450	73841	70783	59929	51210
5	64099	70206	68183	57566	50094
6	62427	68006	65708	55924	48855

In the effusion simulations discussed so far, the size of the target was fixed, so now we investigate the effect of target dimensions. It was found that the average particle path length and number of collisions with surfaces increase linearly in each of the following three cases.

1) The outer diameter is increased and the inner diameter and the target length are kept constant (inner diameter of 5 cm, target length of 25 cm). In this case, the "thickness" of the target (that is the distance between the two cylindrical target walls) is increasing. This case is shown in Figure 11.
2) The inner and the outer diameters are increased by an equal amount, and the length of the target is kept constant (25 cm). In this case, the "thickness" of the target (the distance between the target cylindrical walls) is kept constant and is 5 cm. This case is shown in Figure 12.
3) The length of the target is increased, but the inner and outer diameters are kept constant at 5 cm and 15 cm, respectively. This case is shown in Figure 13.

This means that the effusion time will increase linearly with target dimensions: target length, target thickness, and target inner diameter. Therefore the target dimensions should be kept as small as possible but need to accommodate the primary target and provide enough volume of UC to obtain a high fission rate.

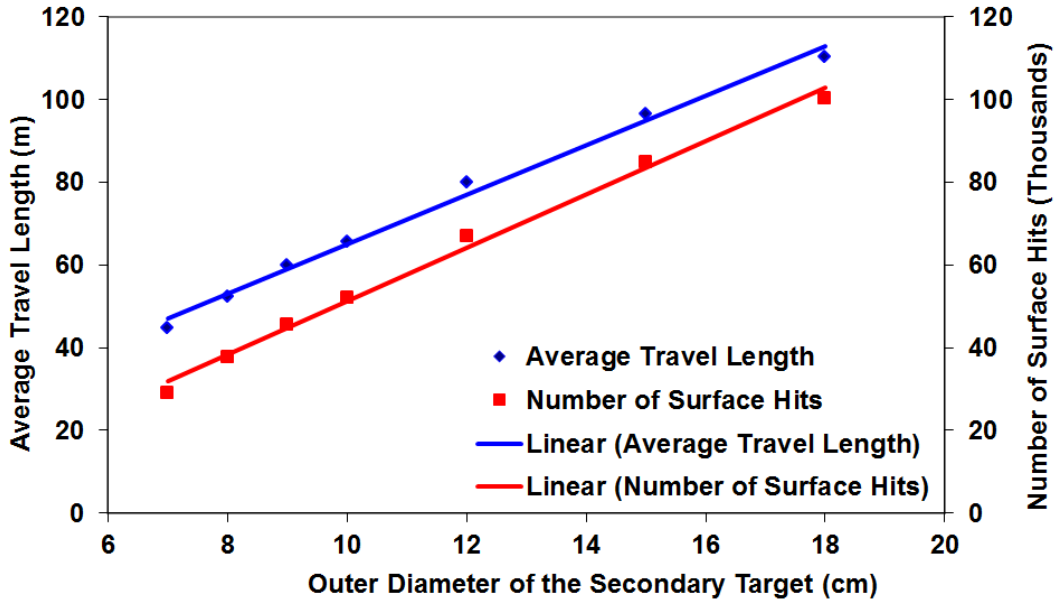

Figure 11. The average travel length and the number of surface hits versus outer diameter of the secondary target (target length 25 cm, inner diameter 5 cm).

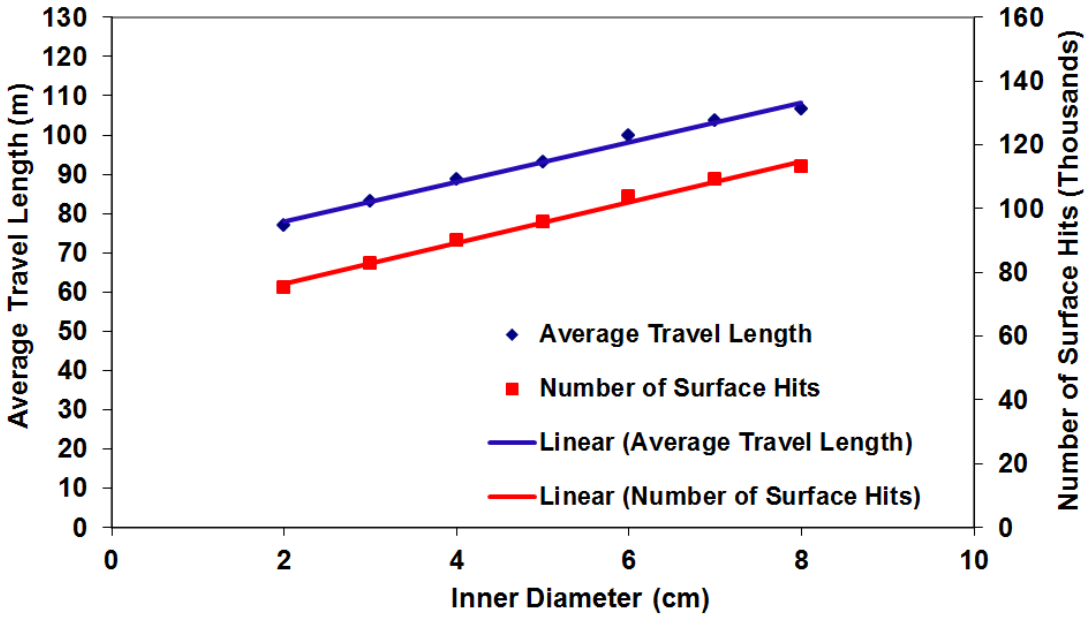

Figure 12. The average travel length and the number of surface hits versus inner diameter of the secondary target. The thickness of the target is kept constant (outer diameter = inner diameter + 10 cm, length = 25 cm).

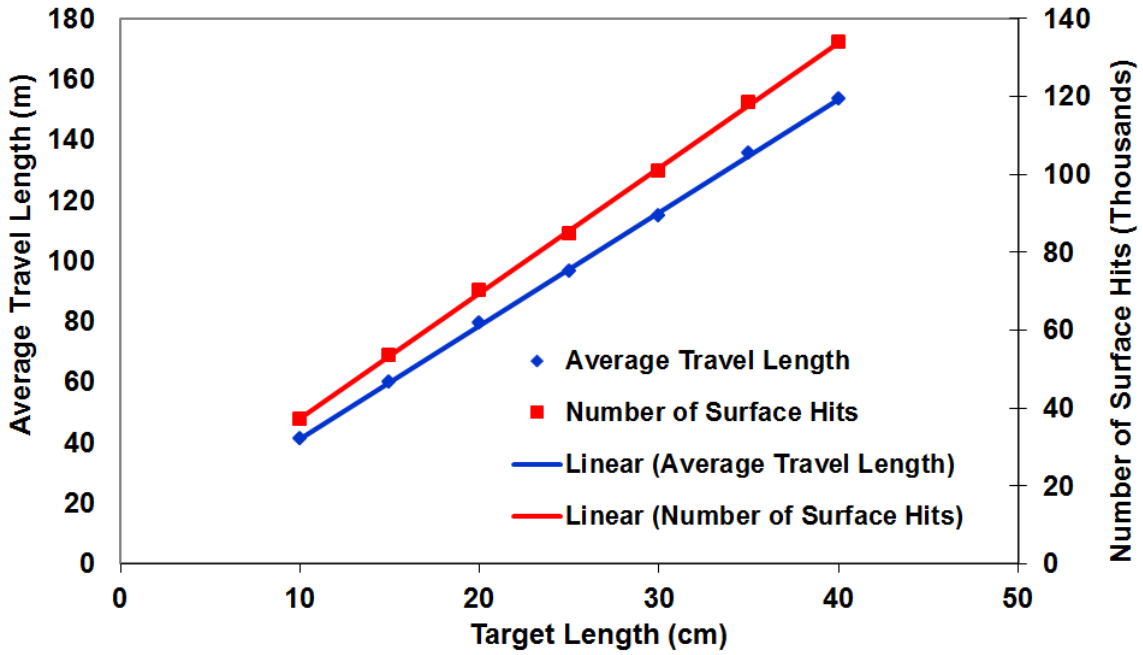

Figure 13. The average travel length and the number of surface hits versus length of the secondary target (inner diameter 5 cm, outer diameter 15 cm).

2.3.3 Effusion Simulations Results for One-Step Targets

For the one-step (direct) targets, we selected our baseline model based on to the actinide target which was under development for the ISAC facility at TRIUMF. Details of the target design were provided by Anne Trudell (ISAC). The target consists of thin foils stacked in the tantalum container. The foils are separated by 0.1 mm gaps and are truncated on the top to provide the effusion path. Each foil consists of a 0.3 mm thick UC_2 layer (density ~6.2 g cm^{-3}) deposited on a 0.13 mm thin exfoliated carbon foil (density 1.5 g cm^{-3}). These composite foils were under development at ISAC for the purpose of improving thermal conductivity. The diameter of the foil is 18 mm, and the foil is truncated 5 mm from the center (so that the height of the cutoff is 4 mm, as sketched in the insert on Figure 16). The stack of the foils is 157 mm long, providing total thickness of ~55 g cm^{-2} of UC_2 and 4.5 g cm^{-2} of carbon. This target will be referred to as the "TRIUMF" target.

An example of the effusion simulations is shown in Figure 14, which depicts the distribution of particles versus distance travelled in the target. The range of the particle paths was divided in 50 equal-width bins; red symbols indicate the number of particles inside the bin; blue symbols indicate the number of particles remaining in the target after travelling the distance given on the abscissa. The simulation was performed for the target configuration as described above for the TRIUMF target, but with a 30 mm radius, 350 mm length, and 7 mm truncation height of the UC_x foils. Figure 15 shows that, as expected, the probability that the particle stays in the target after travelling distance l can be well approximated with a simple exponential distribution of the form Exp(-l/L), where L denotes the average distance that the particle travels. The simulation results in Figure 15 are those from Figure 14; the average travel length L was obtained from the effusion simulation results in Figure 14 (L = 137 m).

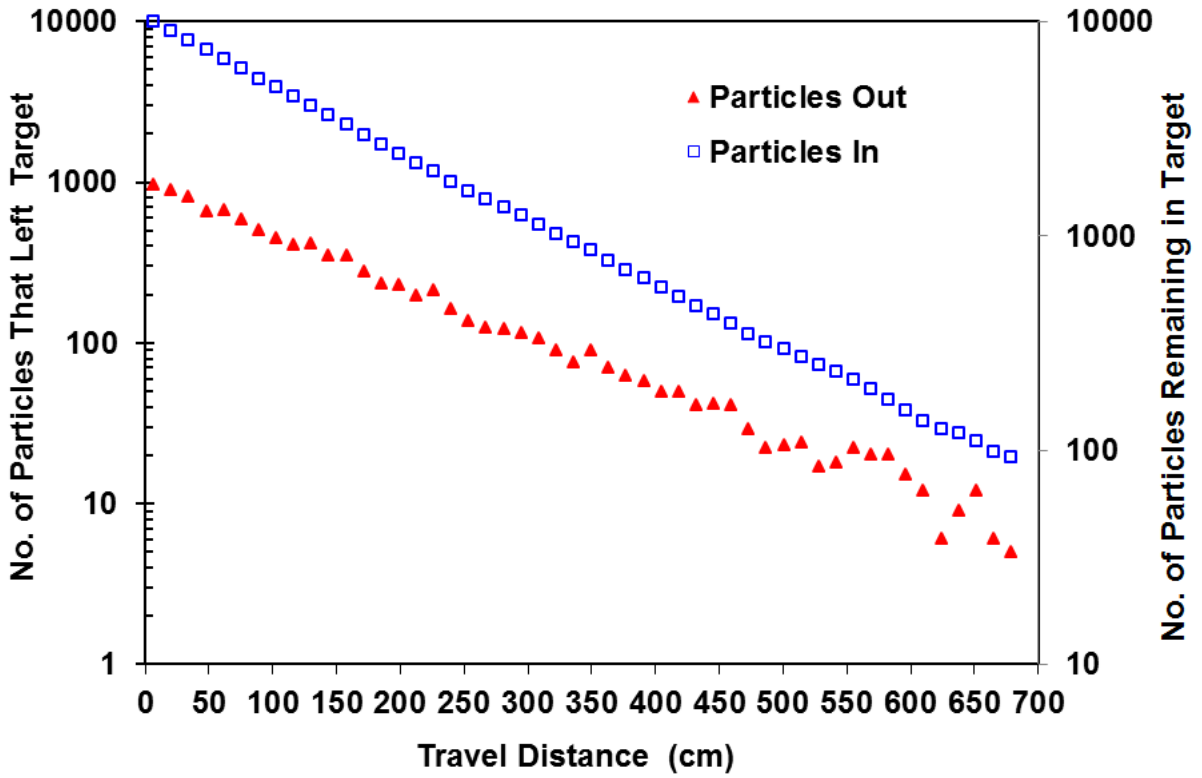

Figure 14. Distribution of particles versus distance travelled in the target. Red symbols denote the number of particles that left the target when they travelled the distance within the bin width around the travel distance given on the abscissa. Blue symbols show the number of particles remaining in the target after they travelled the distance given on abscissa. Simulation was performed for 10,000 particles.

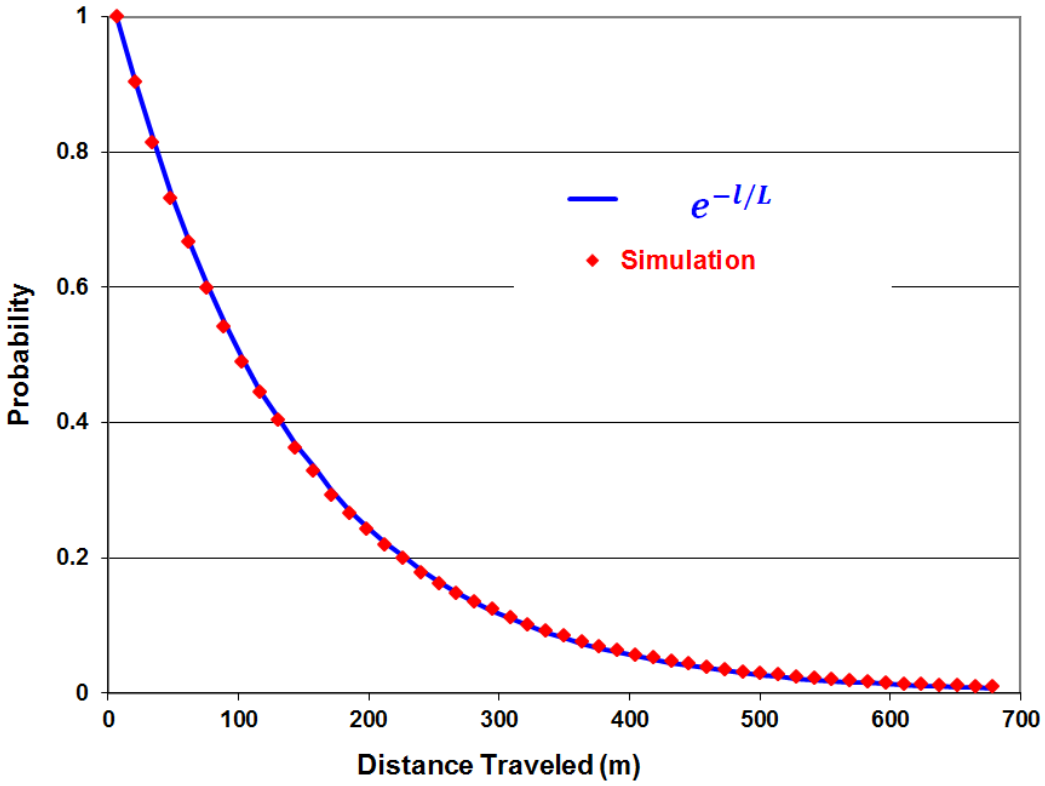

Figure 15. Probability that the particle stays inside the target versus distance travelled. Red symbols depict probabilities obtained directly from the effusion simulation, and the blue line is the exponential distribution Exp(- *l*/*L*), where *L* denotes the average distance travelled, which was obtained from the simulation.

Results of effusion simulations of the TRIUMF target, but with different heights of the foil cutoff, are shown in Figure 16, which depicts the average effusion length and the average number of particle collisions with the surface as a function of the foil cutoff height H. The average effusion path length increases by ~65%, and the number of collisions doubles if the truncation length is reduced from 5 mm to 2 mm. A change from 5 mm to 4 mm cutoff increases the average path length by ~ 12% and the number of collisions by ~ 20%. Cut heights larger than 5 mm bring only little improvement.

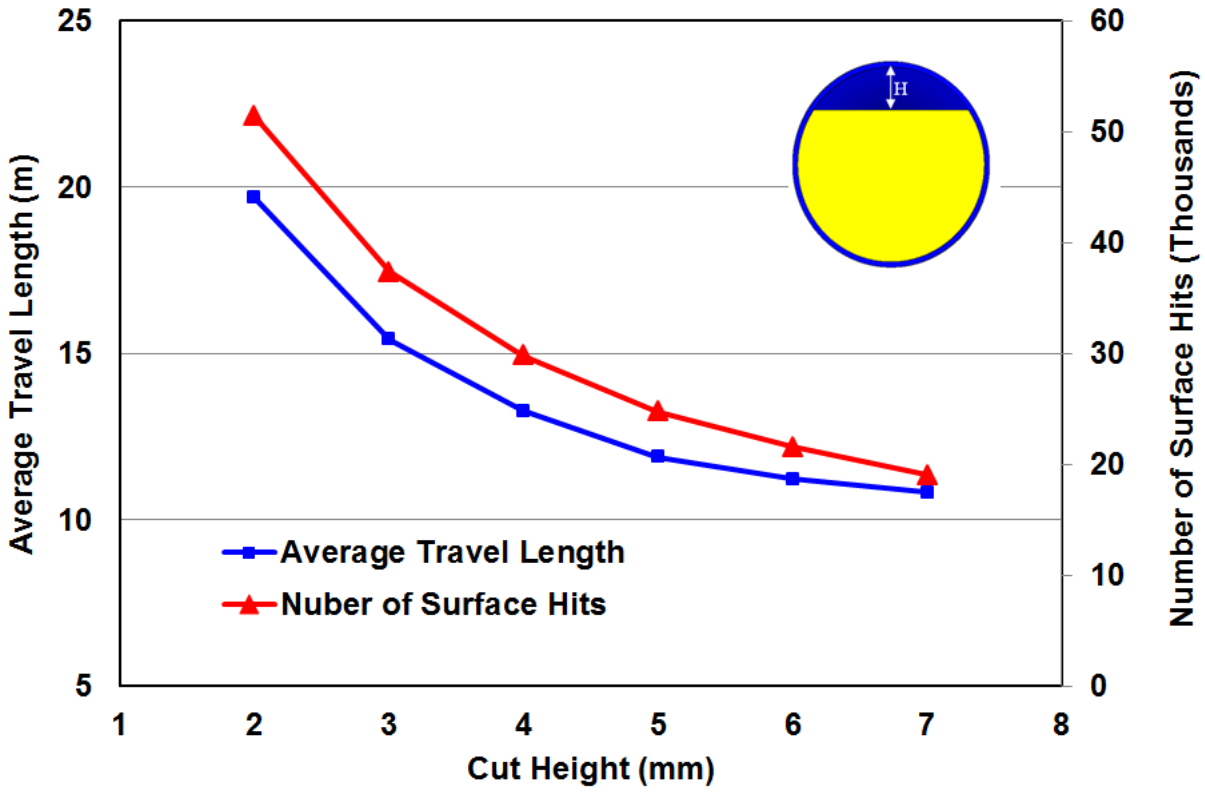

Figure 16. Average travel length and number of collision with surfaces versus foil cutoff for the TRIUMF target.

The effect of the foil cutoff height, for TRIUMF-type targets 15 cm long and with 1 cm, 2 cm, and 3 cm radii is further illustrated in Figure 17, which shows the average travel length versus cutoff height, and Figure 18, which shows the average number of particle collisions with surface versus cutoff height. Results again indicate that a cutoff should be in the range of 4–5 mm. For cutoffs larger than 5 mm, the travel length and the number of collisions do not change much so that the average time the particle stays inside the target remains approximately constant. Larger cutoffs of course also reduce the mass of target material.

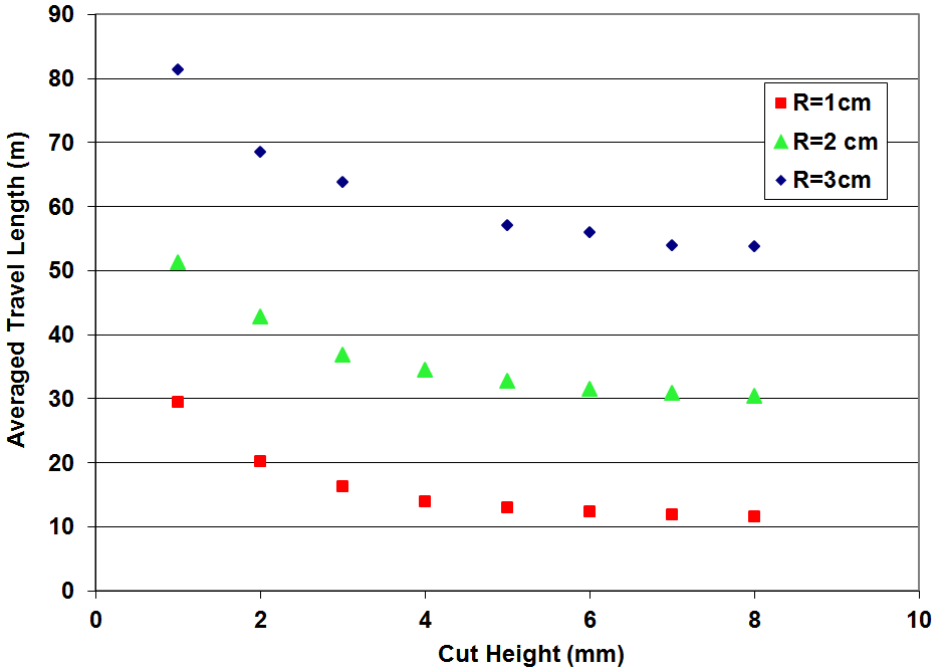

Figure 17. Average travel length versus cutoff height for TRIUMF-type targets 15 cm long and with 1 cm, 2 cm, and 3 cm radii.

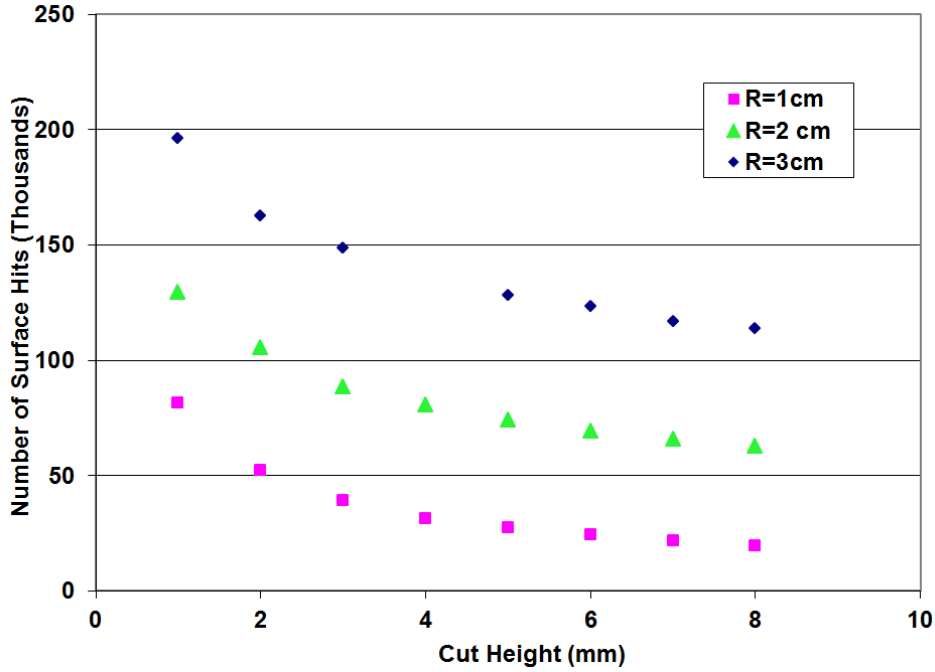

Figure 18. Average number of particle collisions with surface versus cutoff height for TRIUMF-type targets 15 cm long and with 1 cm, 2 cm, and 3 cm radii.

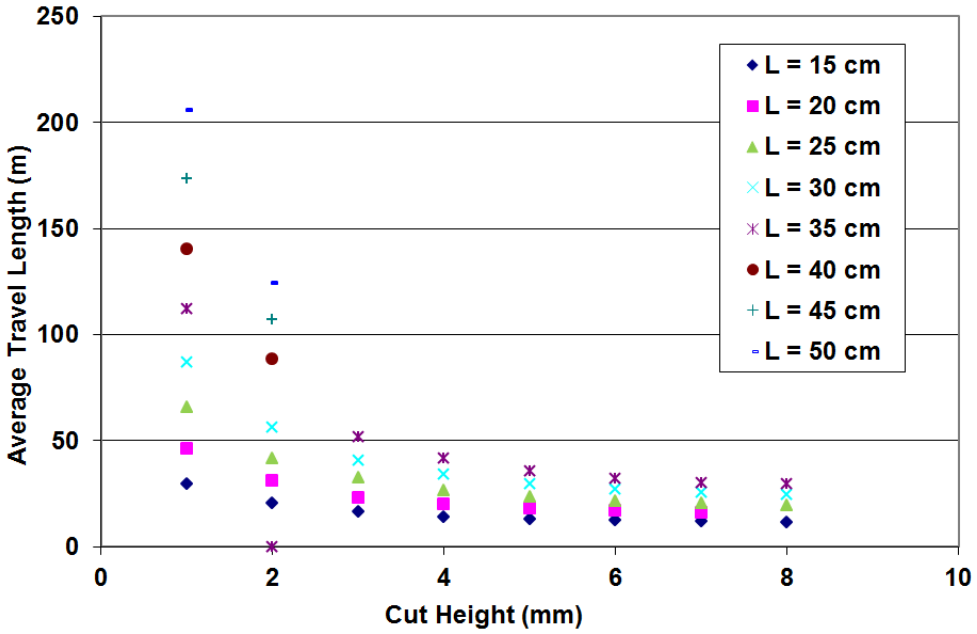

Figure 19. Average path length of a particle versus foil cutoff height, for TRIUMF-type target with radius of 1 cm and length in the range of 15 cm to 50 cm.

Variation of the average path length with the target length and the foil cutoff height for a TRIUMF-type target with radius 1 cm is shown in Figure 19. For the target lengths in the range from 15 cm to 50 cm, it appears that a cutoff of ~4 mm is sufficient.

The variation of average path length with target length, for different cutoff heights, and for a target with radii 1 cm, 2 cm, and 3 cm is shown in Figures 20, 21, and 22, respectively. For all three targets, the average path length increases linearly with increasing target length, and the increase is steeper for smaller cutoffs. The curves for the 4 mm and 6 mm cutoffs are relatively close together, indicating again that cutoffs larger than 4–5 mm are not necessary.

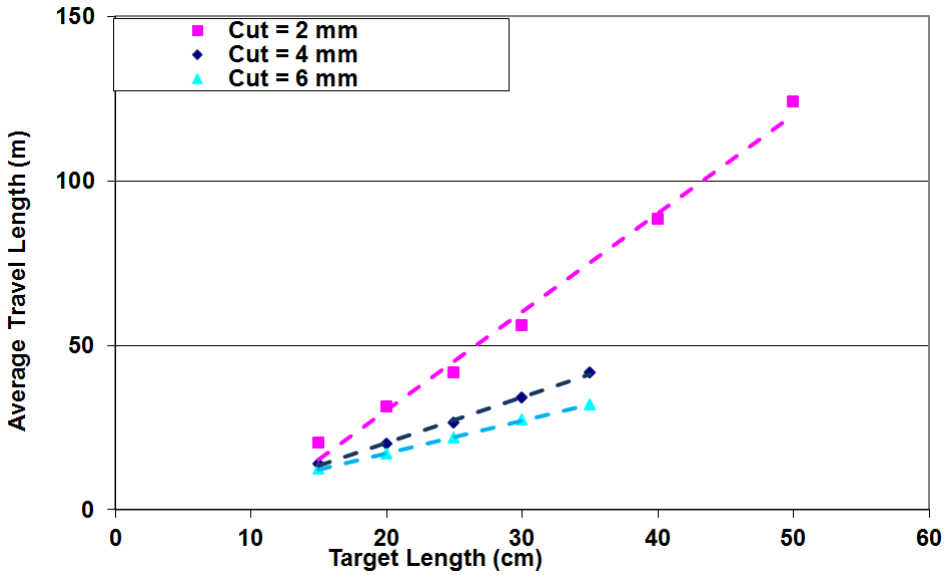

Figure 20. Average particle path length versus target length for three cutoff values. Target radius is 1 cm.

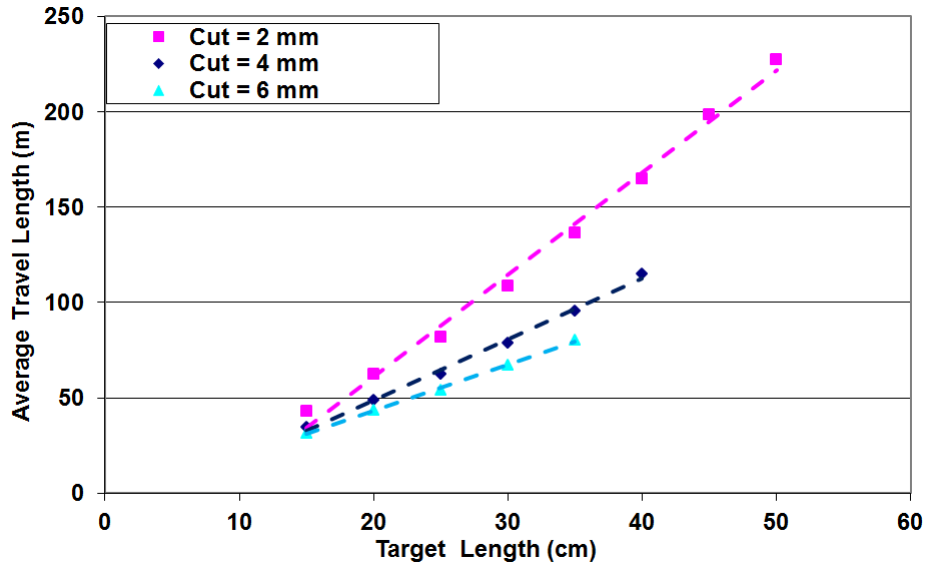

Figure 21. Average particle path length versus target length for three cutoff values. Target radius is 2 cm.

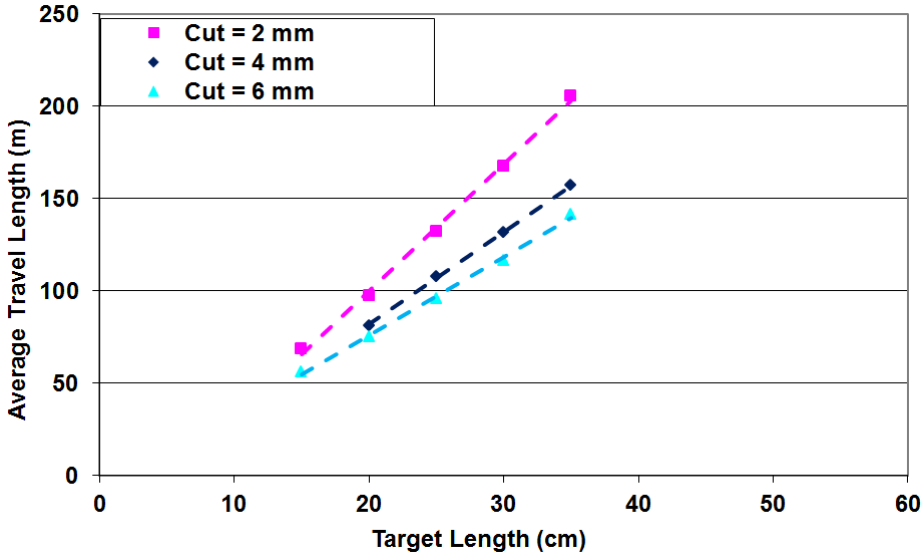

Figure 22. Average particle path length versus target length for three cutoff values. Target radius is 3 cm.

Finally, Figures 23 and 24 illustrate that the average path length and number of collisions with surfaces increase linearly with increasing target radius, for a fixed target length and cutoff height.

The outcome of these investigations for TRIUMF-type direct targets filled with tightly packed foils is that the average effusion length increases linearly with target length and radius and the cutoff in the range of 4–5 mm is sufficient to facilitate effusion.

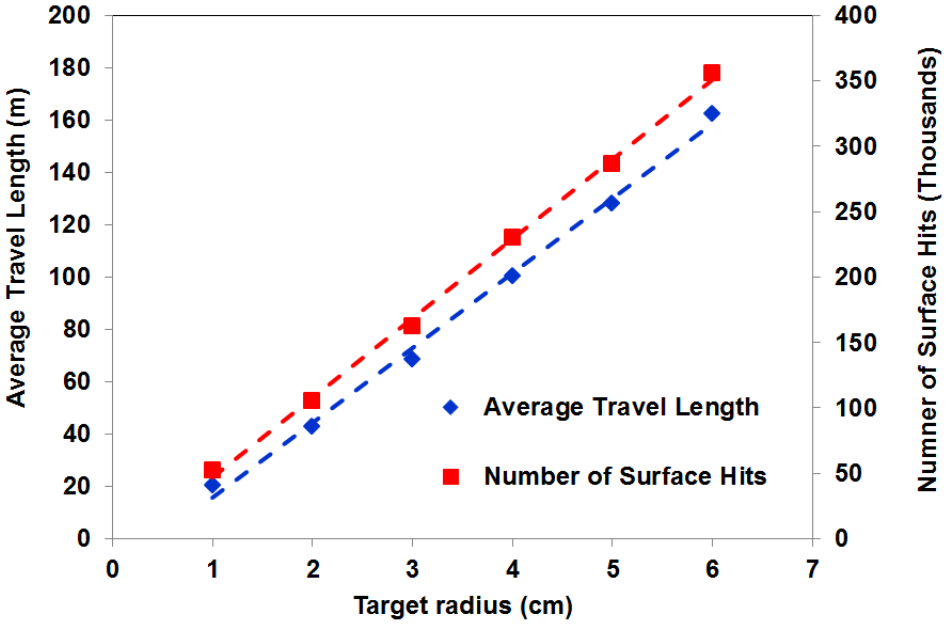

Figure 23. Average particle path length and number of collisions with surfaces versus target radius. The target length is 15 cm, and the cutoff height is 2 mm.

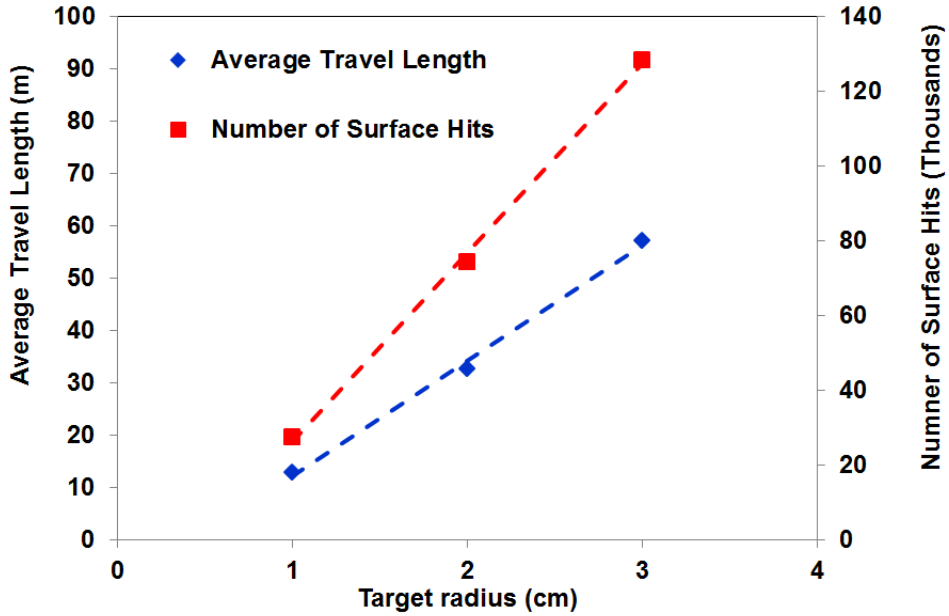

Figure 24. Average particle path length and number of collisions with surfaces versus target radius. The target length is 15 cm, and the cutoff height is 5 mm.

2.3.4 Diffusion Simulations Approach

Starting from Fick's second law of diffusion for stable particles within the homogeneous target material and adding the decay term for unstable particles and production rate term, the diffusion process for a radioactive isotope of concentration C and decay constant λ can be described by the equation

$$\frac{\partial C}{\partial t} = D \cdot \nabla^2 C + S - \lambda \cdot C \,, \tag{4}$$

where D is the diffusion coefficient and S is the production rate of the isotope [19]. The diffusion coefficient D depends on the physical and chemical properties of the diffusion couple − the diffusing particle and target material − and temperature.

For homogenous material targets operated at uniform temperature, constant production rate, and zero initial concentration conditions, the above partial differential equation (PDE) has analytic solutions for the following simple target geometries: one-dimensional planar thin films and slabs, cylinders (infinitely long), and spheres. Analytic solutions to Eq. (4) can be derived by separation of variables and the Fourier transform techniques.

Thin film:
$$I(t) = \frac{2SD}{d^2} \cdot \sum_{k=0}^{\infty} \left\{ \frac{1 - e^{-\left[\frac{D\cdot(k+0.5)^2\cdot\pi^2}{d^2} + \lambda\right]\cdot t}}{\frac{D\cdot(k+0.5)^2\cdot\pi^2}{d^2} + \lambda} \right\} \,, \tag{5}$$

Thin slab:
$$I(t) = \frac{8SD}{d^2} \cdot \sum_{k=0}^{\infty} \left\{ \frac{1 - e^{-\left[\frac{D\cdot(2k+1)^2\cdot\pi^2}{d^2} + \lambda\right]\cdot t}}{\frac{D\cdot(2k+1)^2\cdot\pi^2}{d^2} + \lambda} \right\} \,, \tag{6}$$

Sphere:
$$I(t) = \frac{\pi^2 \cdot SD}{a^2 \cdot \sum_{k=1}^{\infty} \frac{1}{k^2}} \cdot \sum_{k=1}^{\infty} \left[\frac{1 - e^{-(\frac{D\cdot k^2\cdot\pi^2}{a^2} + \lambda)\cdot t}}{\frac{D\cdot k^2\cdot\pi^2}{a^2} + \lambda} \right] \,, \tag{7}$$

Cylinder:
$$I(t) = \frac{SD}{a^2 \cdot \sum_{k=1}^{\infty} \frac{1}{J_{0,k}^{\,2}}} \cdot \sum_{k=1}^{\infty} \left[\frac{1 - e^{-(\frac{D\cdot J_{0,k}^{\,2}}{a^2} + \lambda)\cdot t}}{\frac{D\cdot J_{0,k}^{\,2}}{a^2} + \lambda} \right] \,, \tag{8}$$

where I is the release rate of particles out of the target surfaces, d is the target thickness, a is the radius, and $J_{0,k}$ is the k_{th} positive root of the Bessel function of order zero.

It is also possible to use analytic solutions to Eq. (4) without the decay term ($\lambda = 0$, for stable isotopes) and then apply radioactive decay [20]. However, in most cases, analytic solutions to Eq. (4) do not exist. Therefore, numerical solutions are used for most practical diffusion problems. For this project, a finite-difference code, *Diffuse II*, was used, which solves the PDE of diffusion with radioactive decay – for planar geometry thin films and slabs, cylindrical, and spherical geometry targets [21].

To verify the accuracy of the *Diffuse II* code, its results were compared with the analytic solutions for targets with simple geometries. As an example, Figure 25 shows the results for ^{133}Sn diffusion release from a thin slab UC_2 target obtained by (1) the analytic solution of Eq. (6) (Analytic), (2) by *Diffuse II* code with decay included (Numeric, diffusion, and decay), and (3) by first calculating diffusion release of a stable isotope and then applying the radioactive decay (Numeric, diffusion, then decay). It is assumed that the production of the isotope starts a time = 0 and is constant at later times. The "step-function" shape for the isotope production rate is assumed for all simulations shown here, except where it is explicitly stated that it is different. The maximum difference between the three solutions is less than 1%. Similar agreements were also achieved for calculations of thin film, spherical, and cylindrical geometry targets. The accuracy of the numerical solutions can be improved by refining spatial mesh and time steps.

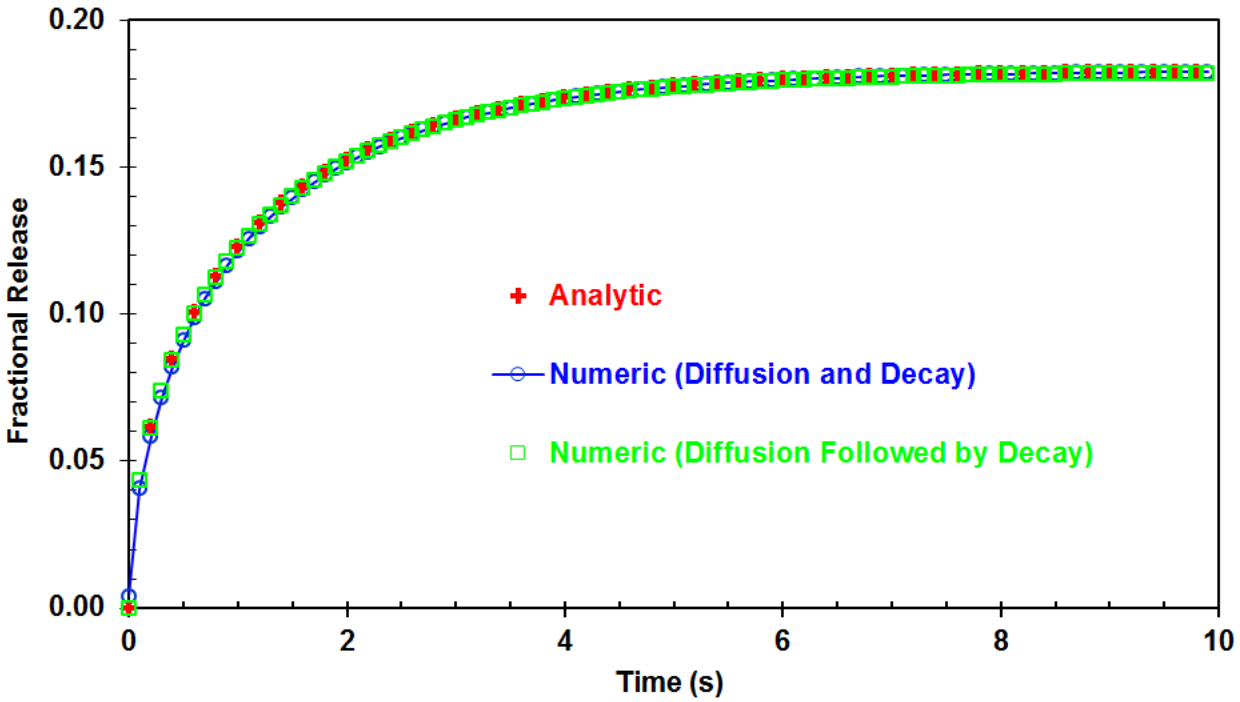

Figure 25. Fractional release of ^{133}Sn ($t_{1/2}$ =1.45 s) from a 5 μm thick UC_2 target slab. Diffusion coefficient of 1.0×10^{-9} cm^2 s^{-1} was assumed. Analytical results are compared with a numerical solution which treats diffusion and decay simultaneously, and with a numerical solution performed for stable nuclide and then corrected for the radioactive decay.

Particle diffusion release strongly depends on the target geometry. Figure 26 shows the fractional yields of ^{133}Sn from four targets with different geometries: spherical and cylindrical targets, with 2.5 μm diameters, and slab and film targets, 2.5 μm thick, simulated with *Diffuse II* code. For the film and slab targets, the analytic solutions are also shown. The same results are displayed in Figure 27, but the target dimensions are increased to 5 μm. Fractional release strongly depends on the size; for 2.5 μm thick film and slab, the fractional release is two times higher than for the 5 μm thick film and slab. For the spherical and cylindrical target, the same change in dimensions leads to 1.57 and 1.75 times larger fractional release. These changes are of course specific for the isotope with a half-life of 1.45 s and diffusion coefficient 1.0×10^{-9} cm^2 s^{-1}.

The effect of the isotope half-life is illustrated in Figure 28, which shows fractional release from a 2.5 μm diameter cylinder for four tin isotopes.

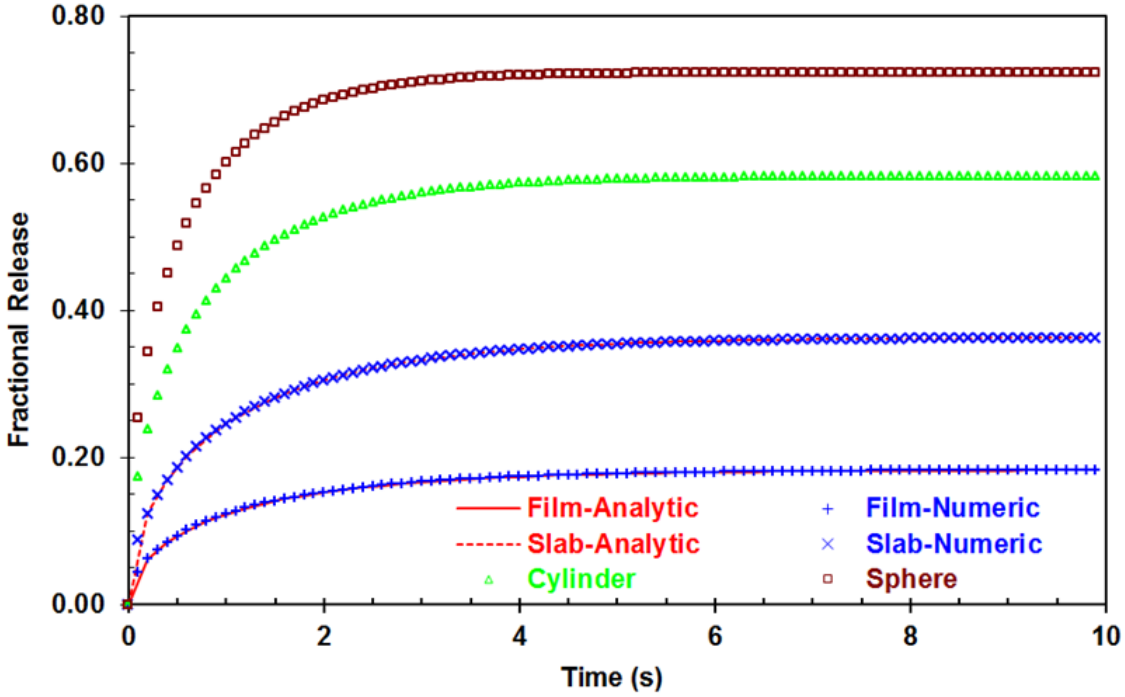

Figure 26. Fractional release of ^{133}Sn ($t_{1/2}$ =1.45 s) from four targets with different geometric shapes. The spherical and cylindrical targets were 2.5 μm in diameter, and slab and film targets were 2.5 μm thick. A diffusion coefficient of 1.0×10^{-9} cm^2 s^{-1} was assumed.

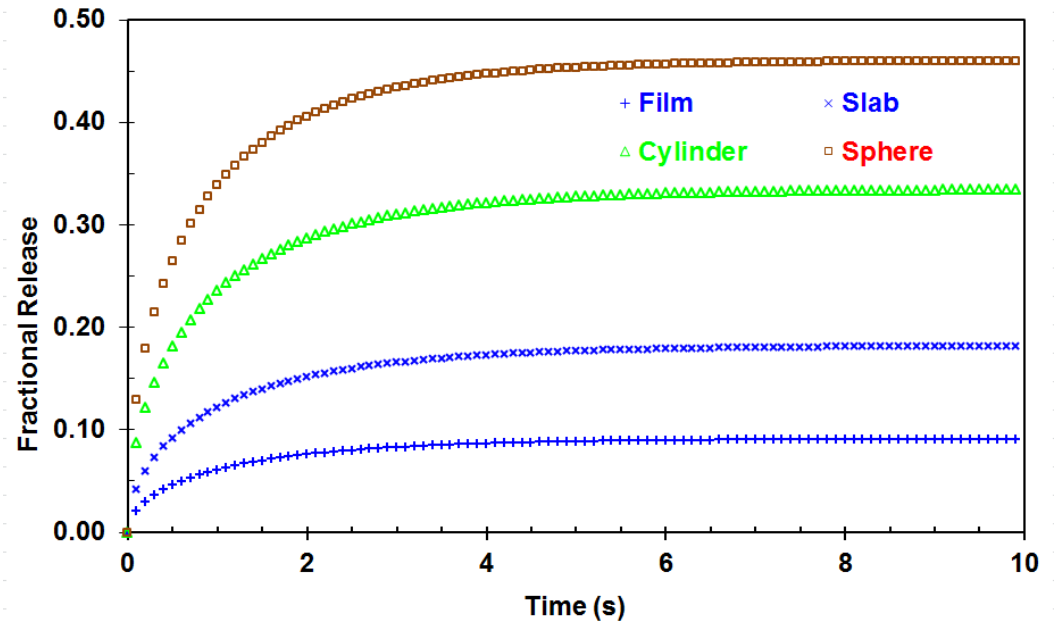

Figure 27. Fractional release of ^{133}Sn ($t_{1/2}$ =1.45 s) from four targets with different geometric shapes. The spherical and cylindrical targets were 5 μm in diameter, and slab and film targets were 5 μm thick. A diffusion coefficient of 1.0×10^{-9} cm^2 s^{-1} was assumed.

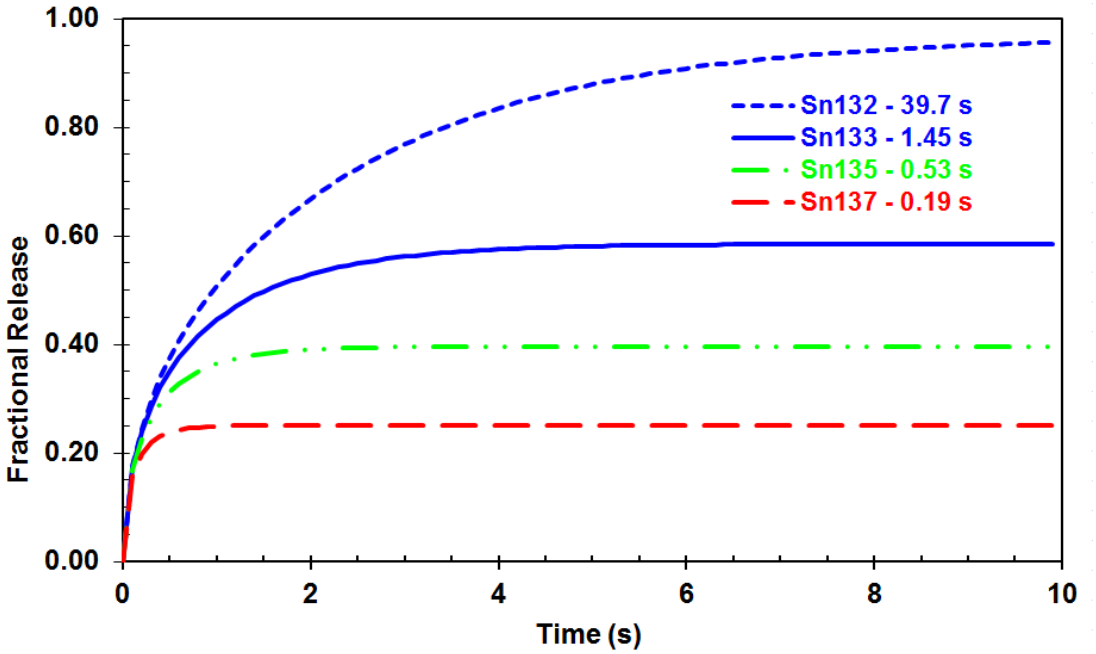

Figure 28. Simulation of diffusion of tin isotopes from cylinder with 2.5 µm diameter. For all isotopes, the same production rate and the same diffusion coefficient (1.0×10^{-9} cm^2 s^{-1}) were assumed.

An attempt to gain insight into the effect of nonuniform temperature distribution in the target is shown in Figure 29. For four selected tin isotopes, the fraction of the isotope released versus time is plotted. Three different temperature distributions inside the target were considered: (a) a uniform target temperature of 2300 K, (b) an average target temperature of 2233 K, with 1/3 of the target at 2300 K and 2/3 at 2200 K, and (c) an average target temperature of 2073 K with 1/15 of the target at 2300 K, 2/15 at 2200 K, 4/15 at 2100 K, and 8/15 at 2000 K. The volumes of the regions at different temperatures were estimated from the heat transfer calculations in which the power deposited in the target was selected so that the maximum temperature did not exceed 2300 K. The release rates were calculated for a 2.5 µm diameter cylinder of UC_x, for each of the temperatures considered. The same diffusion constants were used for all isotopes. The diffusion constant values were assumed to be 1.8×10^{-10} cm^2 s^{-1} at 2000 K, 3.37×10^{-10} cm^2 s^{-1} at 2100 K, 5.98×10^{-10} cm^2 s^{-1} at 2200 K, and 1.0×10^{-9} cm^2 s^{-1} at 2300 K. The release curves for the target were obtained as weighted averages of the release curves for the specific temperature regions (uniform production rate in the target was assumed).

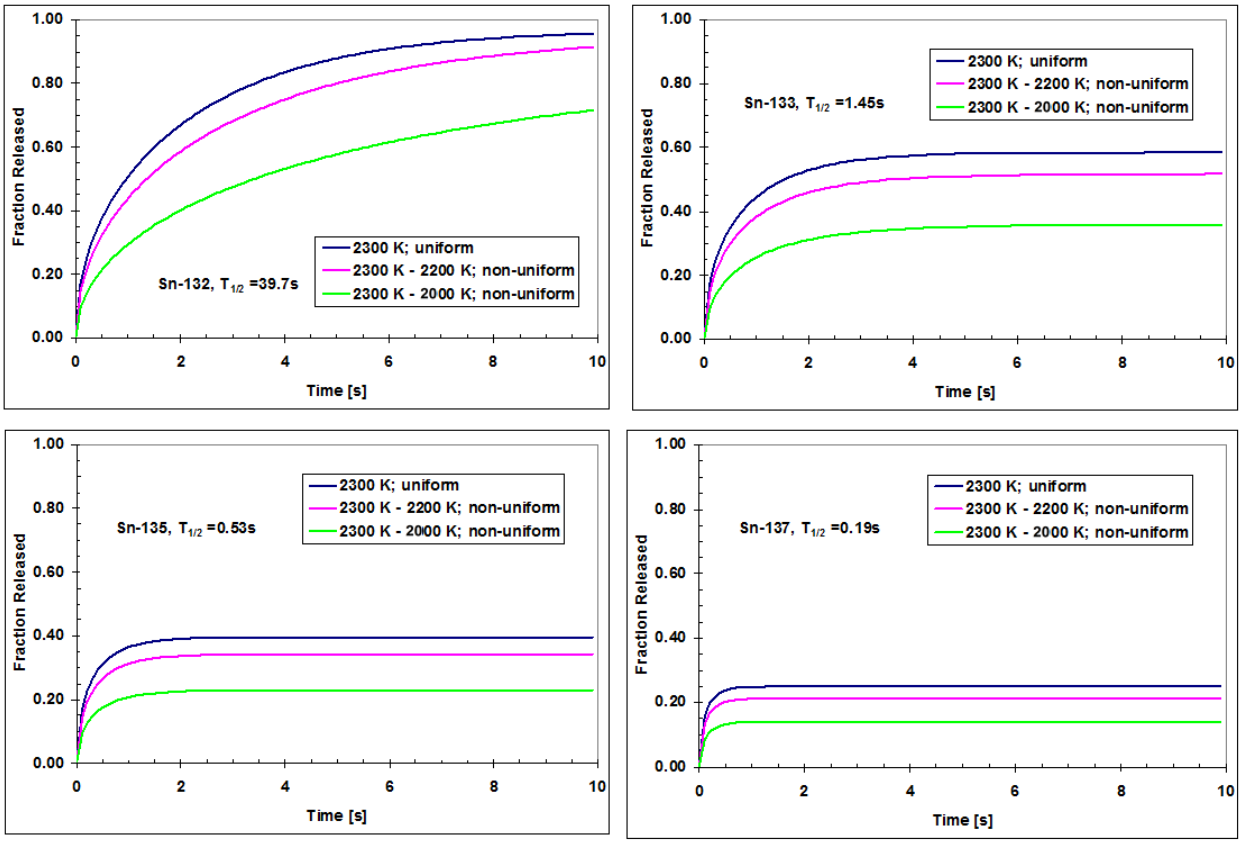

Figure 29. Fractional release for four tin isotopes for the target at uniform temperature and nonuniform temperature distribution with temperature variations of 100 K and 200 K.

The analysis clearly shows the decrease of fractional release of the isotopes with decreasing average temperature of the target and nonuniform temperature distribution. However, the results should be viewed as an example only, because they are very sensitive to the actual temperature-dependent diffusion coefficients of the specific isotopes in the target material.

The diffusion coefficient depends on the physical and chemical properties of the diffusing particle and the target material − and the temperature. Target materials may come from different manufacturers and their properties, such as density, composition, and grain size, which are critical to the diffusion process, may vary significantly. We found that the lack of diffusion coefficients for UC_x target materials is one the most important obstacles for advancing ISOL target optimizations through simulations.

2.3.5 Combining Diffusion and Effusion Simulations

The particle yield *Y*, which takes into account decay losses during the effusion phase, can be calculated analytically, as shown in Eq. (9), for the special case when the diffusion release rate of particles from the target surfaces is in the form of a step function [22]:

$$Y(t) \approx \frac{I}{1+t_C \cdot \lambda} \cdot [1 - e^{-(\lambda + \frac{1}{t_C}) \cdot t}] \ . \qquad (9)$$

I is the diffusion release rate from the target surfaces ($I = 0$ for $t < 0$, and constant *I* for $t \geq 0$) calculated by *Diffuse II* code, or from Eqs. (5–8), with radioactive decay in the diffusion phase included. The constant t_C is the characteristic delay time for effusion through the target system calculated with the *Effusion* code or from vacuum conduction theory.

In more general cases, when the diffusion release rates of particles from the target surfaces are not constant, numerical approximations can be applied to compute the transient curves of particle release. Figure 30 shows the fractional yield rates of ^{133}Sn from a slab UC_2 target for three effusion delay times. The lines (labeled "Numerical") are obtained by applying a histogram (staircase) approximation to the time-dependent $I(t)$ from Eq. (6), and then integrating contributions from individual time steps numerically; by refining the time grid, the accuracy can be improved as needed. The dotted curves (labeled "Eq. 9") are obtained by simply inserting the time-dependent $I(t)$ from Eq. (6) in Eq. (9). While the dotted curves are obviously approximate, Figure 30 shows that they agree quite well with the accurate numerical solutions and are correct at long times when the diffusion release rate $I(t)$ approaches its constant asymptotic value.

Figure 31 shows the particle release curves calculated for a pulsed production mode with an effusion delay of $t_C = 2.0$ s and without it. Isotope production is assumed constant in time intervals of 0–8 s, and zero after that. The diffusion release rate $I(t)$ is computed with *Diffuse II*. With the procedure described here, when the geometry of the target matrix, the diffusing particle, the production rate, the diffusion coefficient, and the characteristic effusion time in the target system are given, the transient release curves of the rare isotope can be calculated accurately. The parameters used in the numerical approximations have explicit and unique physical meaning, which is different from the pulse shape fitting approach described in Ref. [23].

Because the input parameters in the simulations have clear physical meaning, it is possible to determine unknown parameters such as diffusion coefficients or surface adsorption times by fitting the simulated particle release curves to the measured ones. This approach could be readily extended to any ISOL facility and may provide a convenient way of determining parameters governing the rare isotopes transport in the ISOL targets.

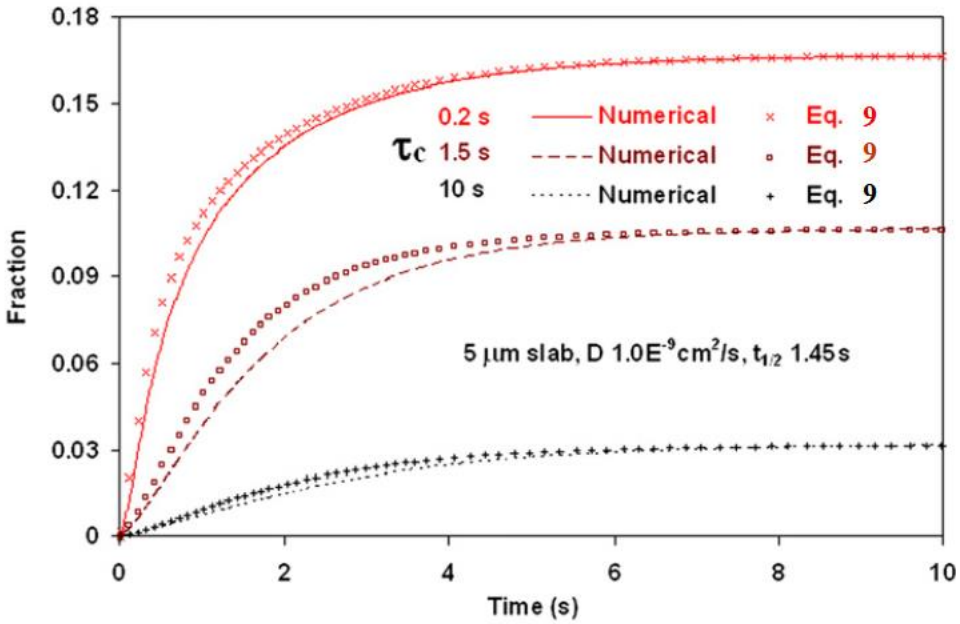

Figure 30. Fractional release rate of ^{133}Sn at different effusion delays: 0.2, 1.5, and 10 s, from numerical simulation (lines) and directly from Eq. (9) (symbols). Diffusion coefficient is 1.0×10^{-9} cm^2 s^{-1}, half-life time is 1.45 s, and the slab target is 5 μm thick.

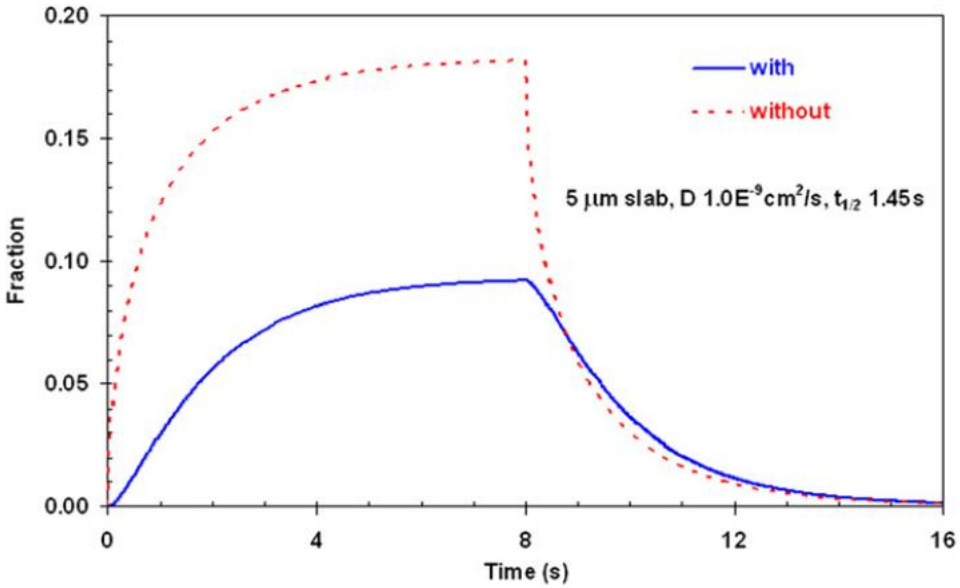

Figure 31. Release curves of ^{133}Sn for a pulsed production mode with and without the effusion delay of t_C = 2.0 s. Diffusion coefficient is 1.0×10^{-9} cm^2 s^{-1}, half-life time is 1.45 s, and the slab target is 5 μm thick.

Figure 32 shows an example of simulated fractional yields compared with experimental results taken from [24] for different K isotopes produced in a fine-powder sintered UC_2 target. In the simulation, we used the diffusion coefficient $D = 2.2 \times 10^{-11}$ cm^2 s^{-1} and the effusion delay $t_C = 2.5$ s.

Simulation studies indicate that 20% uncertainty in the particle production rate and 1% error in the rare isotope current result in ~5% uncertainty in the diffusion coefficient and ~10% uncertainty in the

characteristic effusion time. An interesting direction for the future work would be to apply the described diffusion–effusion simulation methodology to extract the physical parameters from experimental release curves.

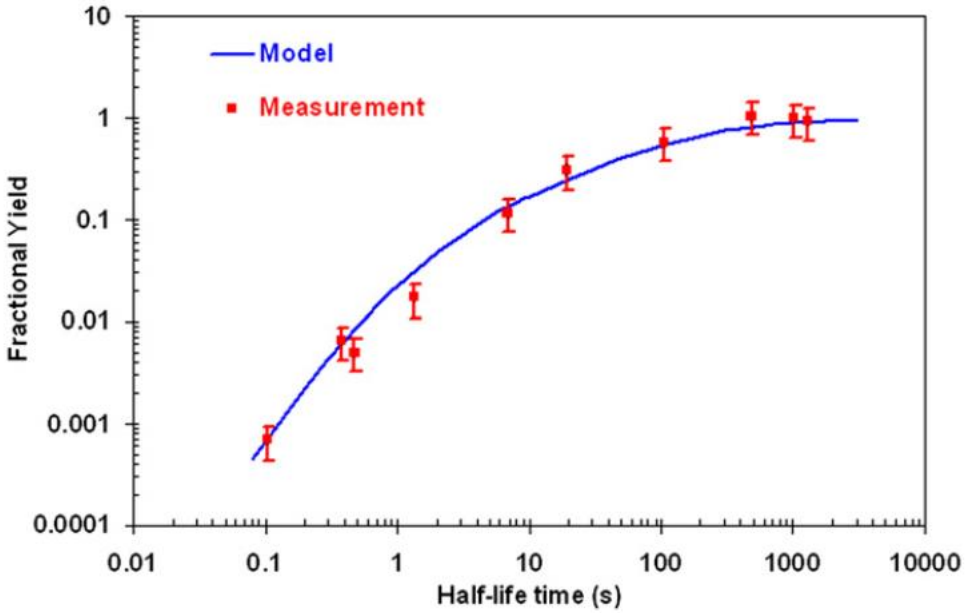

Figure 32. Fractional yield of K isotopes in sintered powder UC_2 target versus isotope half-life time. Simulations (labeled "Model") assumed diffusion coefficient 2.2 × 10^{-11} cm^2 s^{-1} and effusion delay of 2.5 s. Measured values are from Ref. [24].

2.4 SIMULATIONS OF BEAM INTERACTION WITH TARGET

The simulations of beam interaction with targets, transport of secondary particles, and heat deposition were performed with the MCNPX and PHITS codes. The agreement between the two codes for the main results of interest, for example, energy deposited per beam particle, was quite good, typically within a few percent and often within 1%. Based on the results from the previous studies, we concentrated on proton driver beams.

2.4.1 Simulations of Beam Interaction with Direct Targets

Our baseline model was the TRIUMF target, as described in Section 2.3.3, which is made up of a tantalum container filled with a stack of foils separated by radial gaps. Each foil consists of UC_2 deposited on a thin exfoliated carbon foil. The foils have a cutoff on one side to facilitate the effusion. The model was built with explicit representation of the foils so that material heterogeneity and geometry were precisely described, as illustrated in Figures 33 and 34. The densities of the materials were 16.654 g cm^{-3} for tantalum, 6.2 g cm^{-3} for UC_2, and 1.5 g cm^{-3} for exfoliated graphite.

Two other targets, one with 20 mm inner radius of the container and the foils and another with 30 mm radius, but otherwise identical to the TRIUMF target, were also analyzed. The parameters of the targets are summarized in Table 7.

The driver beam was a 500 MeV mono-directional proton beam, with a Gaussian radial profile. The full-width at the half-maximum (FWHM) was 6 mm for the TRIUMF target and was increased for the larger target so that the FWHM-to-target-radius ratio for the TRIUMF target was maintained (Table 7). For the two larger targets, the height of the cutoff was increased only to 5 mm because the effusion studies indicated that larger cutoffs are not necessary.

The results are summarized in Tables 8 and 9; statistical uncertainties of the results were typically small (less than ~2%) and are not reported here. Relative to the 9 mm target at the same driver-beam power, the target with a 2 cm radius produces ~29% more fission and 23% higher energy deposition, while the target with 3 cm radius produces 42% more fissions and 32% higher energy deposition. Energy deposition distributions in the targets are shown in Figure 35. Statistical uncertainties associated with individual mesh-interval energy deposition values were small, typically less than a few percent. Larger targets have the beam spread over larger area, which results in lower peak heating density. This can be confirmed by inspecting the scales at the right side in Figure 35; the maximum value shown in the scale for the target is the peak heating rate in the target.

Table 9 gives the number of fissions per second for the 500 MeV proton beam power of 5 kW, 10 kW, and 20 kW. The fission rate of the target increases linearly with the driver beam power; however, the maximum fission rate attainable by the target and the corresponding driver-beam power that can be sustained by the target is limited by the amount of heat that can be dissipated by the target. This will be investigated in Section 2.5.

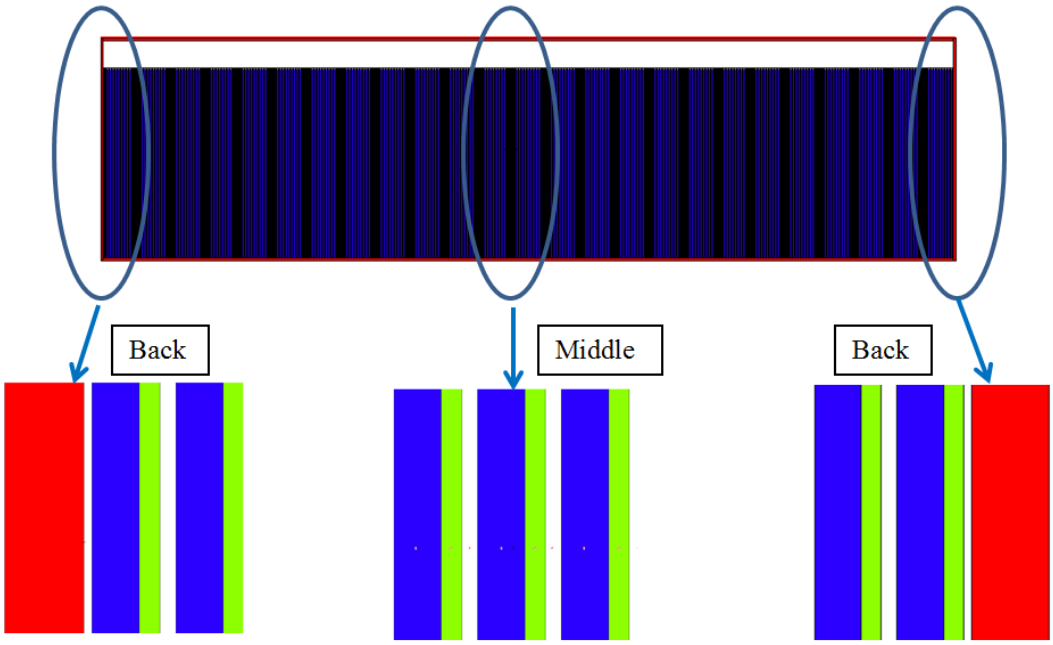

Figure 33. Longitudinal section through TRIUMF target model (top), with details of the front end, middle, and back end sections. Tantalum is red, UC_2 is blue, and exfoliated carbon is green. The gaps between the container and the first foils and the container and the last foil are 0.05 mm thick. Gaps between other foils inside are 0.1 mm thick. Tantalum container is 0.5 mm thick. Foil consists of 0.30 mm thick UC_2 layer on 0.13 mm thick carbon foil-backing.

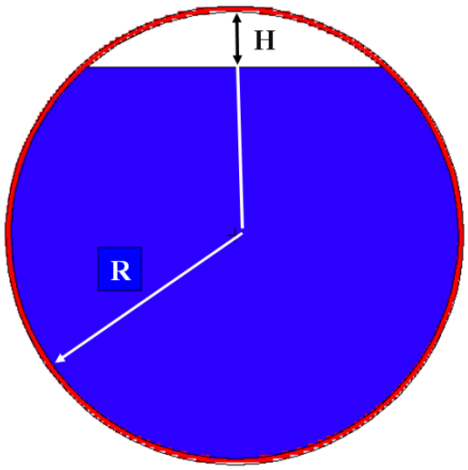

Figure 34. Section through the target perpendicular to the beam direction. H denotes the cutoff height, and R is the radius.

Table 7. Dimensions of the targets analyzed

Target	Inner radius R (mm)	Cutoff height H (mm)	Beam FWHM (mm)
9 mm (TRIUMF)	9.00	4.00	6.00
20 mm	20.00	5.00	13.33
30 mm	30.00	5.00	20.00

Table 8. Target heat deposition and fission rate per proton for three targets

Target	Target heat (MeV/proton)	No. fissions per proton	Target heat/ beam power (%)
9 mm	112	0.149	22.4
20 mm	138	0.192	27.6
30 mm	148	0.212	29.5

Table 9. Total number of fissions at selected beam powers for the three targets

Target	Number of fissions/s in target at proton beam power		
	5kW	10kW	20kW
9 mm	9.31E+12	1.86E+13	3.72E+13
20 mm	1.20E+13	2.40E+13	4.81E+13
30 mm	1.33E+13	2.65E+13	5.30E+13

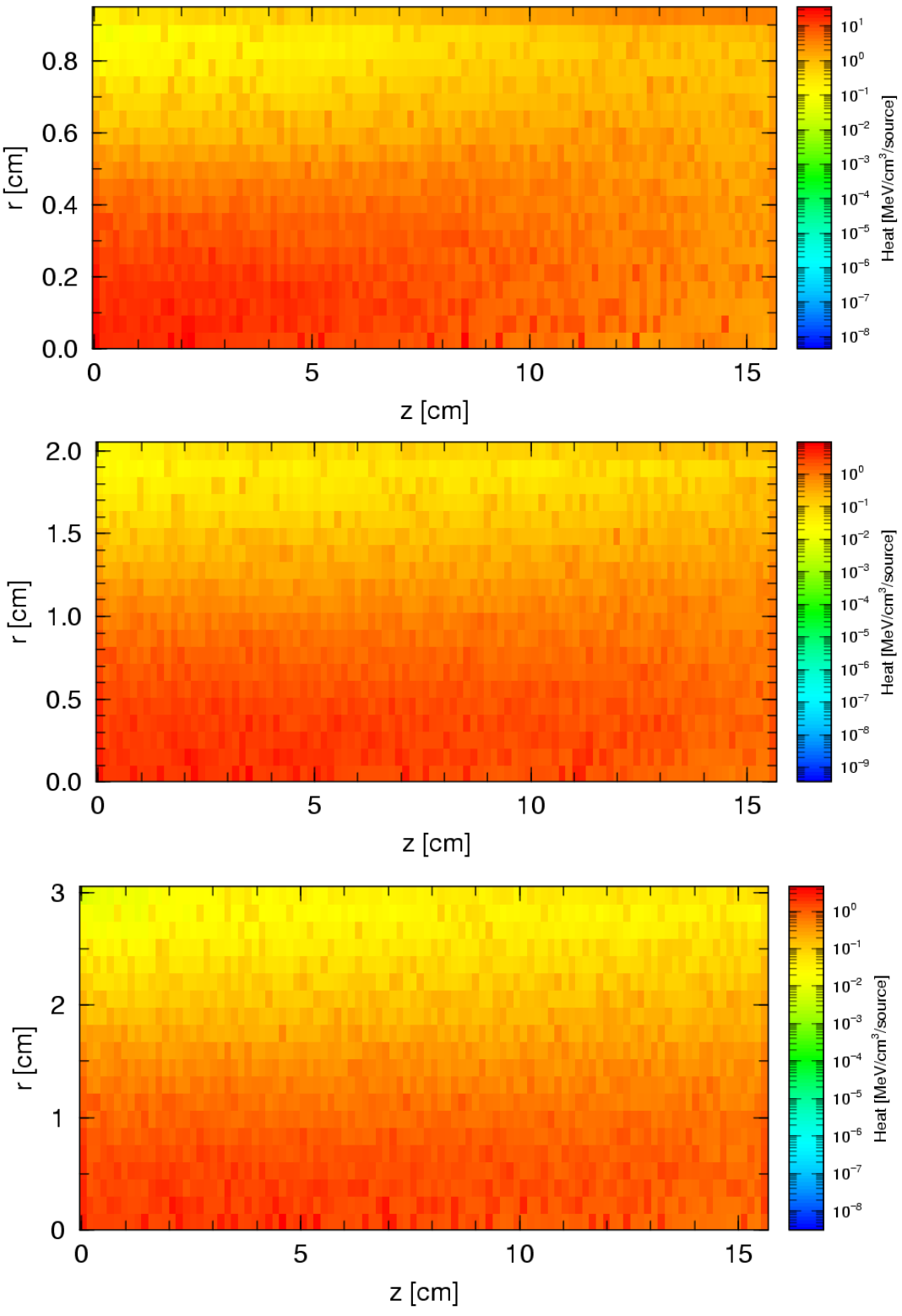

Figure 35. Distribution of the energy deposition in the targets: target with 30 mm radius is at the top, 20 mm radius is in the middle, and 9 mm radius is at the bottom. Because of the large aspect ratio of the targets, the plots are stretched in vertical (that is radial) direction.

2.4.2 Simulations of Beam Interaction with Two-Step Targets

For two-step targets, only a few simulations of beam interaction with targets were performed with detailed target models. Figure 36 shows an example of a model, which consisted of a primary target made of tungsten with 10% by volume water enclosed in a 0.1 mm thick stainless-steel container. The primary target is 20 cm long and has a 1.27 cm inner radius. There is a radial gap from 0.37 cm to 1.55 cm between the primary and the secondary target. The secondary target is housed in a 0.5 mm thick tantalum hollow-cylindrical container, with a 1.60 cm inner radius and a 6.60 cm outer radius. The 5 cm thick space between the cylindrical walls is filled with "TRIUMF-type" UC_2/C foils, with exactly the same composition and thickness as those used in direct target investigations. However, here the foils have the shape of hollow cylinder with a 6.59 cm outer radius and a 1.60 cm inner radius. There is a 0.1 mm thick gap between the outer edge of the foils and the tantalum container. The axial spacing (empty space) between foils is 0.1 mm.

Results for a series of calculations in which the effect of the length and position of the primary target was investigated are shown in Table 10. The configuration of the targets was as described above and shown in Figure 36; the changes –mainly in the primary target position and length – are listed in Table 10. The position of the primary target is given relative to the secondary target, which starts at 0 cm. Figure 37 depicts fission density distributions for the targets listed in Table 10.

Statistical uncertainty of the integral quantities (e.g., number of fission per proton) were typically less than ~1%, and for the energy deposition distributions, the uncertainty for individual mesh intervals values were typically a few percent.

Further work on two-step targets was not possible because of the funding limitations.

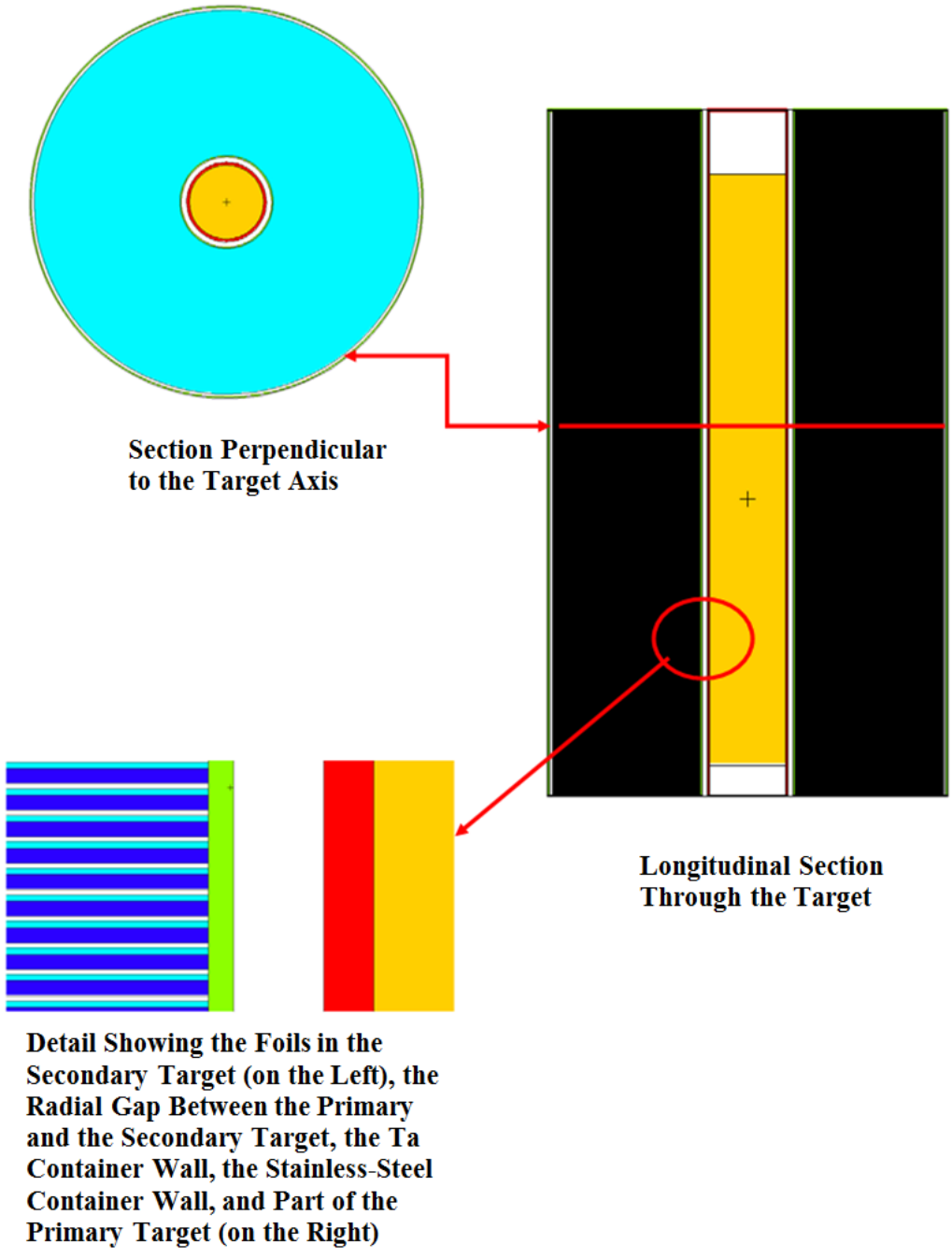

Figure 36. An example of a two-step target model.

Table 10. Variations of two-step targets with different primary target lengths and positions (number of fissions per proton are also given)

Target label on Figure 37	Primary target length (cm)	Primary target position (cm)	Secondary target length (cm)	Number of fissions per proton
(a)	10	5–15	25.0	0.367
(b)	15	5–20	25.0	0.426
(c)	20	2–22	25.0	0.456
(d)	20	1–21	23.213	0.437

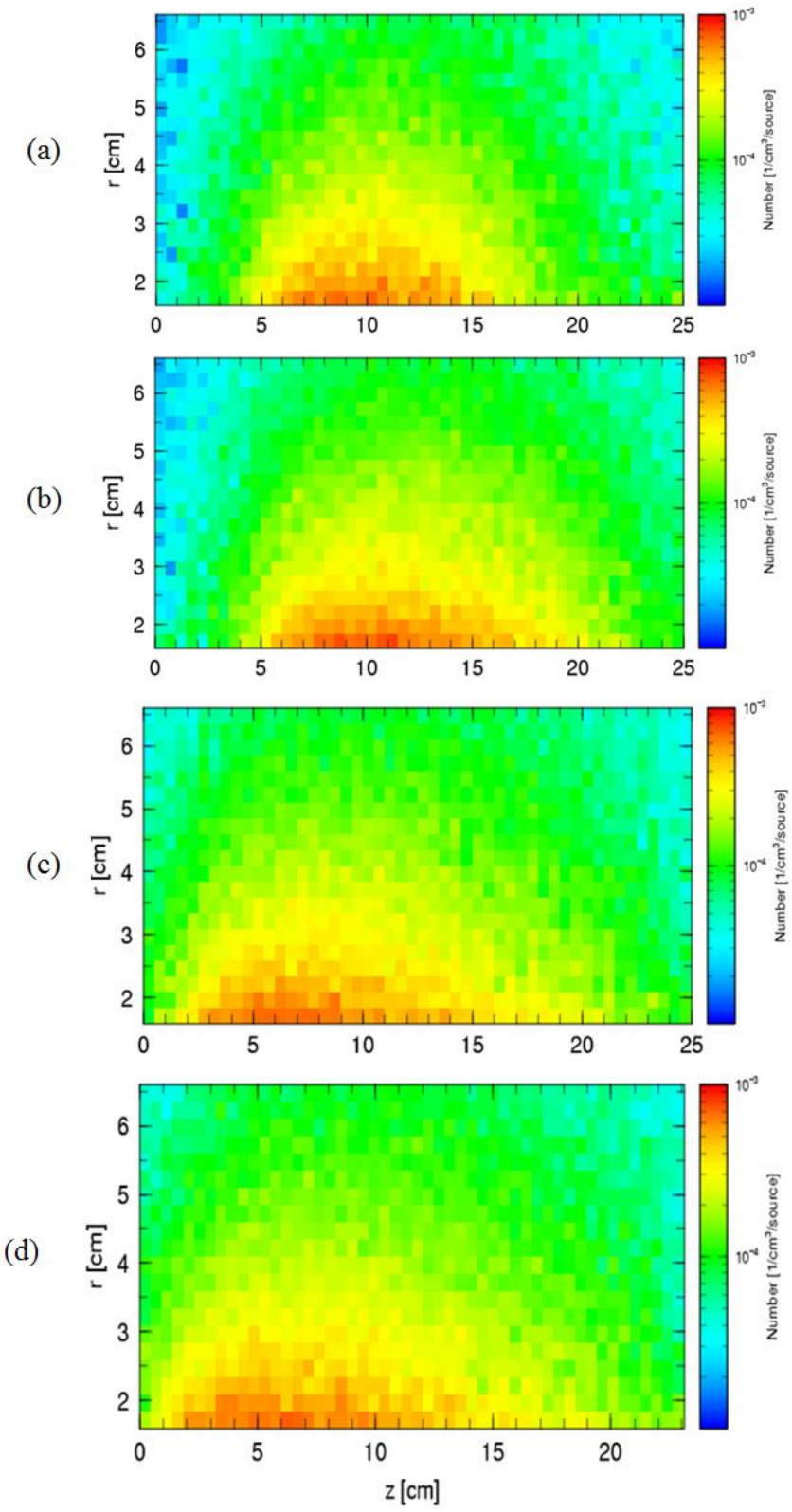

Figure 37. Fission density distribution in the secondary target for the targets listed in Table 10. Calculations explored the effect of the length and position of the primary target.

2.5 SIMULATIONS OF HEAT TRANSFER

Heat transfer calculations were performed for the three direct targets, which were described in Section 2.4.1. Detailed geometry models were constructed with explicit representation of foils, UC_2 and C layers, gaps between foils, and tantalum container. Computer code *HEATING 7.2* was used for all calculations. Estimated temperature-dependent conductivity for UC_2 at reduced density was obtained from [14], which also provided temperature-dependent conductivity for exfoliated graphite foils. The target was cooled only by thermal radiation from the tantalum container to the environment, assumed to be at room temperature (20°C). The energy deposition distributions obtained from simulations of primary beam interactions with targets were used. As discussed in Section 2.4.1, the driver beam was a 500 MeV proton beam.

Figure 38 shows an example of the temperature distribution in the target with radius 9 mm, for the beam power 10 kW. The temperature profile along the target axis, at the target centerline, is depicted in Figure 39 for the three targets considered, at the beam power 10 kW. Larger targets allow larger beam radii – for the 9 mm target, the Gaussian profile of the proton beam had 6 mm FWHM, and for the larger two targets, the beam FWHM was increased proportionally with the radius increase. This results in lower maximum energy deposition and lower maximum temperature.

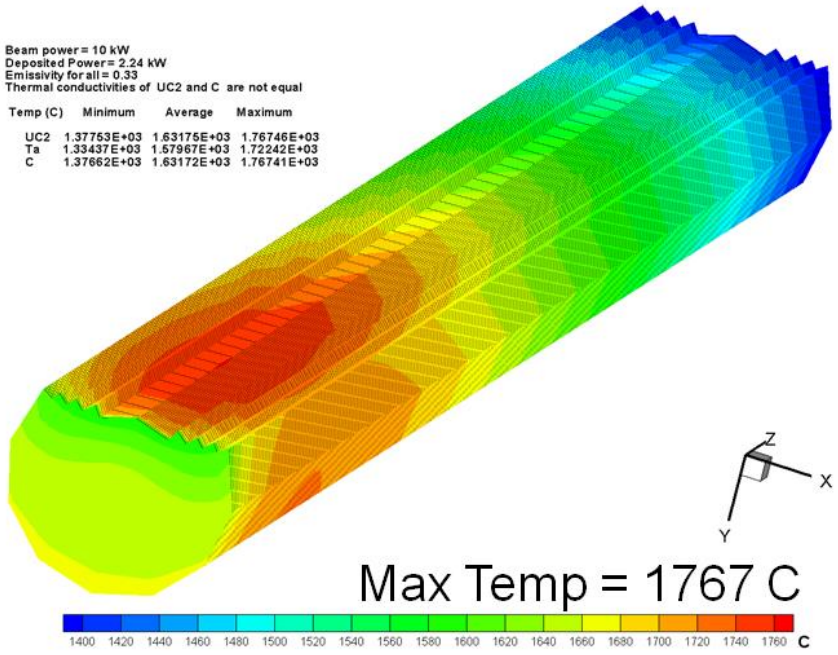

Figure 38. Temperature distribution in the target with radius 9 mm, bombarded with 10 kW proton beam with proton energy 500 MeV. Energy deposited in the target is 2.24 kW. Tantalum cover is removed to expose the inside of the target. Maximum temperature in the target is 1767°C.

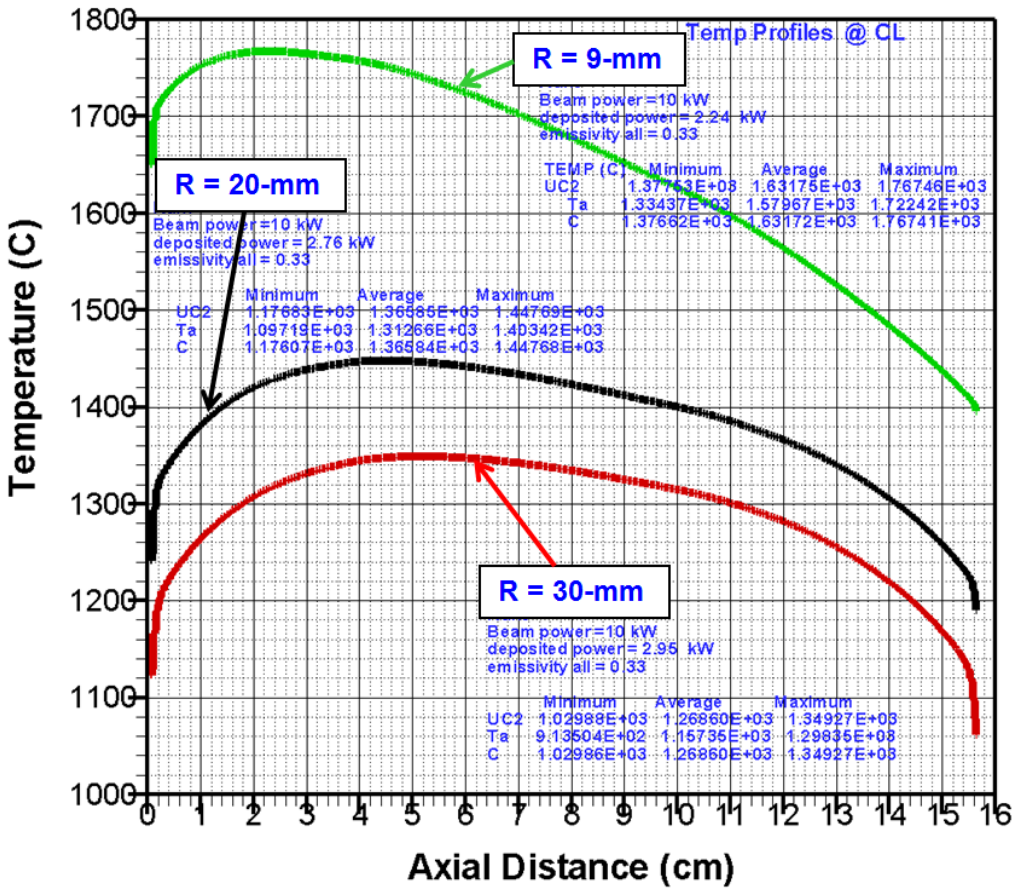

Figure 39. Temperature versus distance from the front of the target, at the target centerline, for the targets with 9 mm, 20 mm, and 30 mm radii.

Energy deposited in the target increases linearly with the beam power (at the constant proton beam energy); however, the maximum temperature does not increase linearly due to the heat transfer effects. This is illustrated in Figure 40. In order to prevent excessive thermal decomposition of UC_2, the maximum temperature in the target must be kept below ~2200°C. This restriction limits the maximum power that can be deposited in the target and, consequently, the maximum driver beam power and maximum fission rate that the target can produce.

For the three targets considered, the temperature calculations were repeated for different beam powers, so that the maximum temperature in UC_2 was brought within ± 25°C of 2200°C. The results are shown in Figure 41. Increasing the target radius by a factor of 3.3, from 9 mm to 30 mm, allows an increase in beam power by only a factor of two. However, the corresponding increase in fission rate is larger— about 2.8 times—and almost linear with target radius, as shown in Figure 42. The reason that the fission rate increases faster with the target radius than the allowed beam power is that there is more UC_2 in larger targets and secondary particles, especially neutrons, produce more fission. The (cumulative) fission yields per proton are therefore larger for larger targets, in this case for targets with larger radii. This is illustrated in Figure 43, which shows the maximum beam power, fission yield per proton, and fission rate versus target radius; all quantities are given relative to the values for a target with a 9 mm radius.

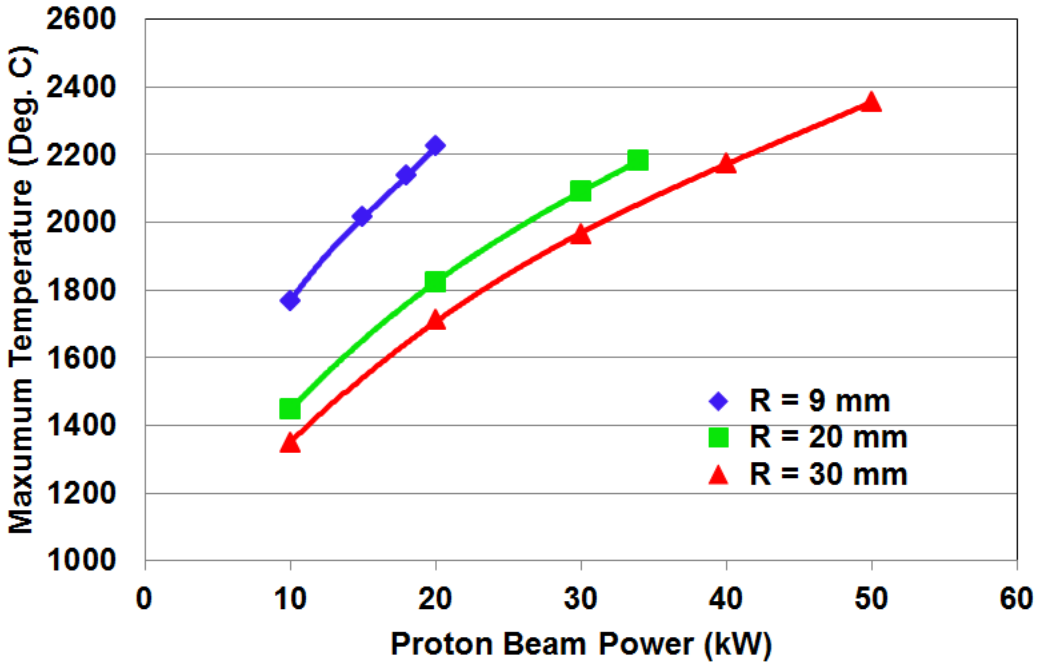

Figure 40. Maximum temperature in UC_2 versus beam power for three targets with different radii (emissivity of 0.33 for all materials).

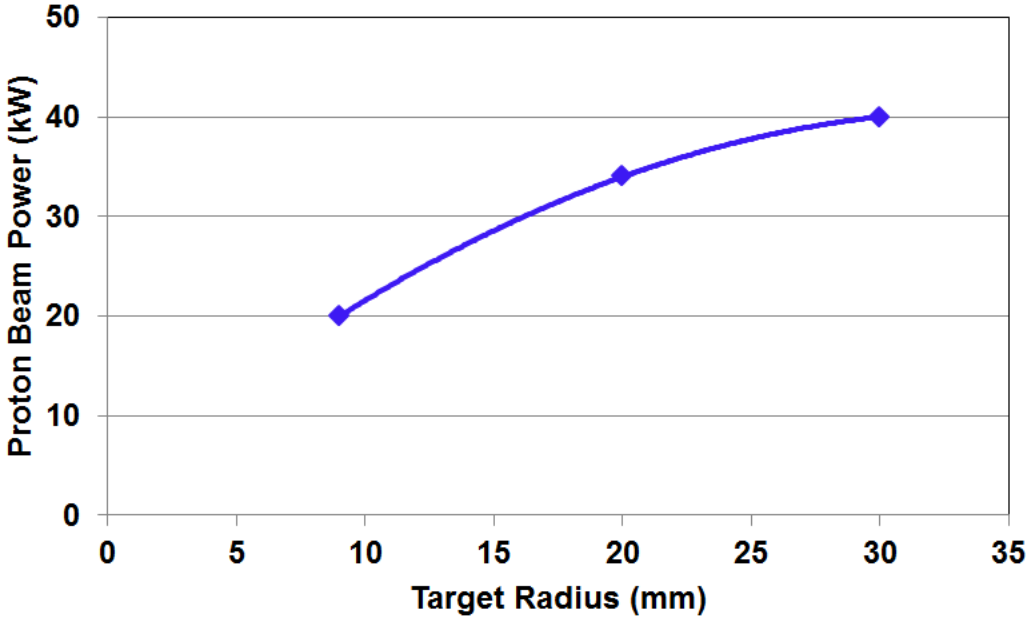

Figure 41. Maximum beam power allowed on target with maximum temperature limited to ~2200°C versus target radius (500 MeV proton beam, emissivity of all materials of 0.33).

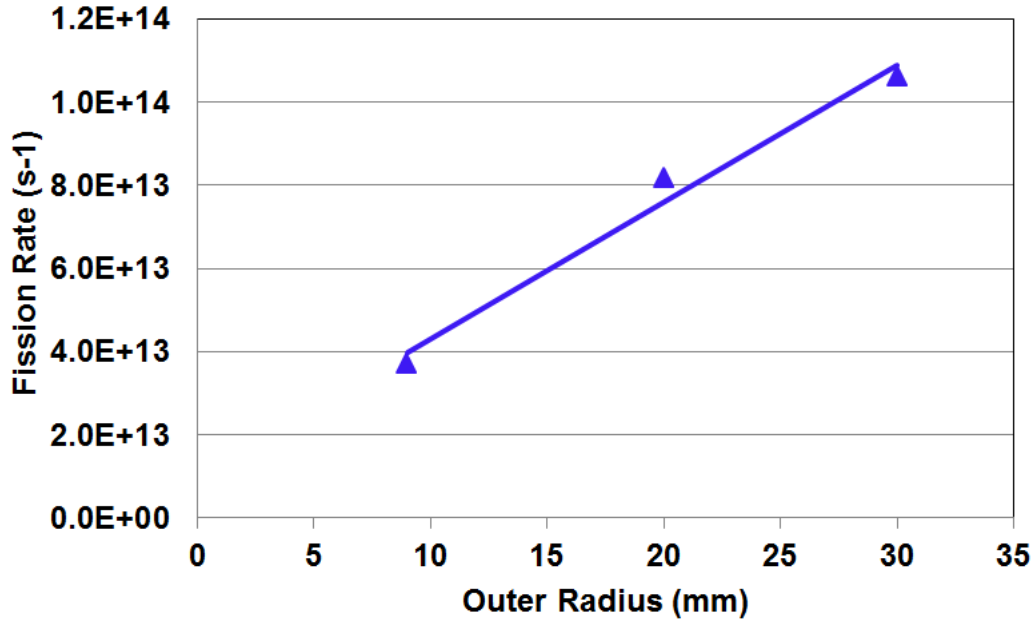

Figure 42. Maximum fission rate versus target radius (same conditions as described for Fig. 41).

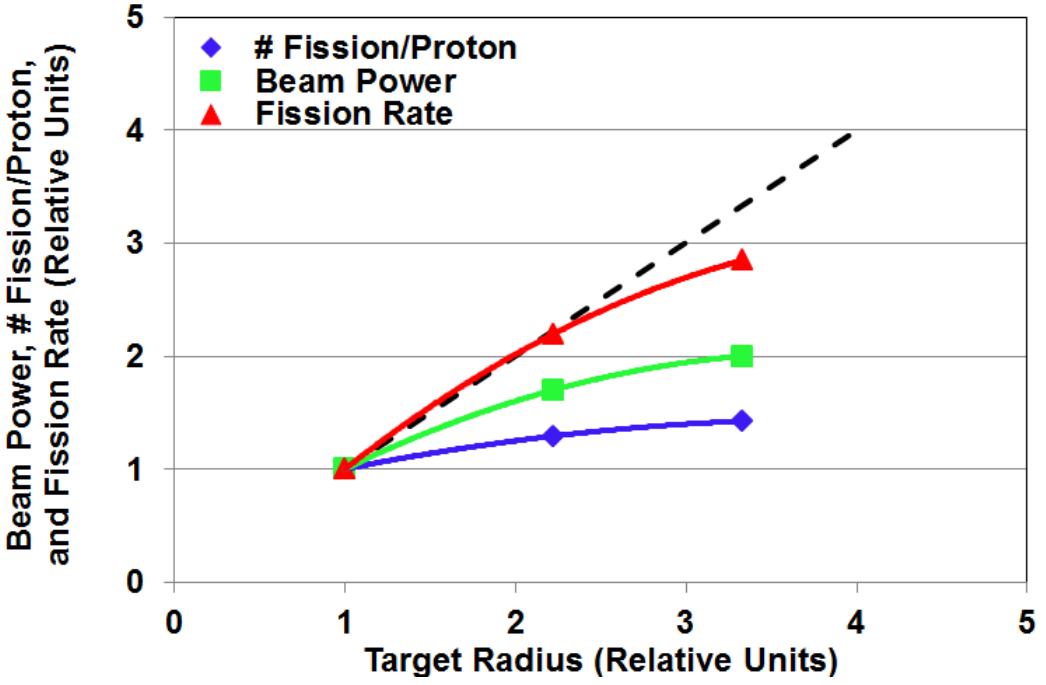

Figure 43. Allowed beam power, fission yield per proton, and fission rate versus target radius. All values are relative to the target with a 9 mm radius.

Because thermal radiation from the tantalum container is the only cooling mechanism for the target, we expected that tantalum emissivity would have a large impact on the maximum beam power allowed on the target. We investigated this effect with a series of heat transfer analysis. The maximum allowed heating of

the target and the beam power were again determined with the constraint that the maximum temperature stays within ± 25°C of 2200°C. The results, depicted in Figure 44 and summarized in Table 11, indeed show a strong increase in maximum allowed beam power with increasing tantalum emissivity. Changing the tantalum emissivity from 0.33 to 1 (black body radiation) allows a beam power increase of about two times for all three targets.

Table 11 gives the maximum allowed beam power, the corresponding heat deposition, and the fission rate for each combination of the target radius and tantalum emissivity considered. Maximum temperature is also listed.

Table 12 lists the allowed beam power, number of fissions per proton, and fission rate, normalized to the values for 9 mm target with tantalum emissivity 0.33. In this way, the relative contributions of the increase in the allowed beam power and the increase in number of fissions per proton with increasing target radius are clearly shown. For example, the target with a 30 mm radius and tantalum emissivity of 1.0 produces a ~5.6 times higher fission rate than the target with a 9 mm radius and tantalum emissivity of 0.33. The increase is a product of two factors; for the larger target, the number of fissions per proton is 1.4 times higher and the allowed beam power is ~ 4 times higher.

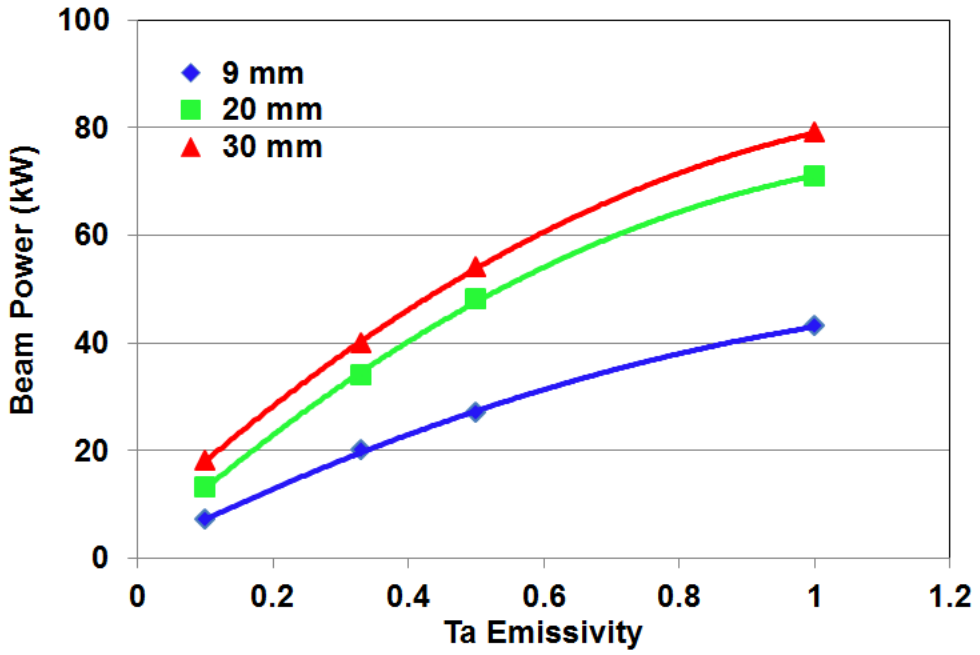

Figure 44. Allowed beam power versus tantalum emissivity for three targets considered. For each emissivity, the beam power is determined so that the maximum temperature in target is within 2200°C ± 25°C.

Table 11. Beam power, target heating, maximum temperature, and fission rate for three targets considered and tantalum emissivity of 0.33 and 1.00

Tantalum emissivity	Target radius	Beam power	Target heating	Maximum temperature	Fission rate
	(mm)	(kW)	(kW)	(°C)	(fissions/s)
0.33	9	20	4.48	2212	3.72 E+13
	20	34	9.38	2182	8.18 E+13
	30	40	11.80	2174	1.06 E+14
1.00	9	43	9.63	2187	8.00 E+13
	20	71	19.60	2188	1.71 E+14
	30	79	23.31	2224	2.09 E+14

Table 12. Number of fissions per proton, beam power, and fission rate for the three targets considered and for a tantalum emissivity of 0.33 and 1.00. All numbers are given relative to the values for the target with a 9 mm radius and tantalum emissivity of 0.33.

Tantalum emissivity	Target radius	Fissions/ proton	Beam power	Fission rate
0.33	9	1.00	1.00	1.00
	20	1.29	1.70	2.20
	30	1.42	2.00	2.85
1.00	9	1.00	2.15	2.15
	20	1.29	3.55	4.59
	30	1.42	3.95	5.63

3. CONCLUSION

The research studied one-step and two-step Isotope Separation on Line (ISOL) targets for future radioactive beam facilities with high driver-beam power through advanced computer simulations. As a target material, uranium carbide in the form of foils was used because of increasing demand for actinide targets in rare-isotope beam facilities and because such material was under development in ISAC at TRIUMF. Simulations of effusion were performed for one-step and two-step targets, and the effects of target dimensions and foil matrix were studied. Diffusion simulations were limited by availability of diffusion parameters for UC_x material at reduced density; however, the viability of the combined diffusion–effusion simulation methodology was demonstrated and could be used to extract physical parameters such as diffusion coefficients and effusion delay times from experimental release curves. Dissipation of the heat from the ion-producing targets is the limiting factor for high-power beam operation both for the direct and two-step targets. Detailed target models were used to simulate proton beam interactions with the targets to obtain the fission rates and power deposition distributions, which were then applied in the heat transfer calculations to study the performance of the targets.

Results indicate that a direct target, with specifications matching the ISAC TRIUMF target, could operate in a 500 MeV proton beam at beam powers up to ~40 kW, producing ~8×10^{13} fission/s with maximum temperature in UC_x below 2200°C. This is much higher than the beam power used so far in the ISAC TRIUMF operation with UC_x targets, which did not exceed 5 kW beam power [25].

Targets with larger radii allow higher beam powers and fission rates. For the target radii in the range of 9 mm to 30 mm, the achievable fission rate increases almost linearly with target radius; however, the effusion delay time also increases linearly with target radius.

4. REFERENCES

1. Argonne National Laboratory, ATLAS, http://www.phy.anl.gov/atlas/.

2. Michigan State University, National Supercomputing Cyclotron Laboratory, http://www.nscl.msu.edu.

3. TRIUMF, http://www.triumf.ca/.

4. Oak Ridge National Laboratory, http://www.ornl.gov/.

5. DOE/NSF Nuclear Science Advisory Committee Report, Robert Tribble (Chair), *The Frontiers of Nuclear Science* (December 2007).

6. Facility for Rare Isotope Beams: http://frib.msu.edu/.

7. G. Bollen, "Rare Isotope Production at RIA," Targetry Workshop, Long Island, 2003.

8. G.W. McKinney et al., "MCNPX 2.7.X—New Features Being Developed," LA-UR-09-6788, IEEE/NSS Conference, Orlando, FL, October 25-31, 2009; http://mcnpx.lanl.gov/.

9. K. Niita, N. Matsuda, Y. Iwamoto, H. Iwase, T. Sato, H. Nakashima, Y. Sakamoto, and L. Sihver, "PHITS: Particle and Heavy Ion Transport Code System," Version 2.23, JAEA-Data/Code 2010-022 (2010); http://phits.jaea.go.jp/.

10. K. W. Childs, *HEATING 7.2 User's Manual*, ORNL/TM-12262, Oak Ridge National Laboratory, Oak Ridge, Tenn., November 1992.

11. ANSYS, Inc., *CFX5.7 Manuals*, Canonsburg, Pennsylvania.

12. Development of a Concept for the ISOL Target Areas for RIA (DE-FG02-04ER41322), http://www.oro.doe.gov/riaseb/docs/Bollen_Status%20report%20RIA%20ISOL_091904.pdf.

13. J. P. Greene, J. A. Nolen, M. Petra, and T. A. Burtseva, "Thermal Conductivity Measurements of Uranium Carbide by Electron Bombardment," Proceedings of AccApp'03, p. 560 (2004) (originally obtained online from http://www.phy.anl.gov/ria/publications/Thermal_Cond.pdf.)

14. M. Dombsky, "Fabrication of ISAC High Thermal Conductivity Composite Target Material," presented at First Workshop on Actinide Target Development, April 27–29, 2006, TRIUMF, Vancouver, British Columbia; personal communication to I. Remec.

15. J. M. Lafferty, *Foundations of Vacuum Science and Technology*, John Wiley and Sons, Inc., 1998.

16. J. C. Bilheux and G. D. Alton, *Nucl. Instr. And Meth. Phys. Res. B*, Vol. 267 (2009).

17. Y. Zhang and G. D. Alton, *Journal of Vacuum Science and Technology*, Vol. A 23, 1558 (2005).

18. GEANT4 is a Monte-Carlo Code for calculating scattering effects, energy loss, and production of secondary particles through nuclear reactions by energetic ion beams, http://geant4.web.cern.ch/geant4/.

19. R. Kirkaldy and D. J. Young, *Diffusion in the Condensed State*, The Institute of Metals, London, 1987.

20. M. Barbui et al., *Nucl. Instru. and Meth. B*, Vol. 266, 4289 (2008).

21. Y. Zhang, G. D. Alton, and Y. Kawai, "Simulation Studies of Diffusion-Release and Effusive-Flow of Short-Lived Radioactive Isotopes" Proceedings of the 21st Particle Accelerator Conference (PAC05) 16-20 May 2005, Knoxville, TN, USA, p. 1739 (available online at http://accelconf.web.cern.ch/AccelConf/p05/PAPERS/TPPE021.PDF).

22. Y. Zhang, I. Remec, and Z. Liu, "ISOL Target–Vapor Transport System Simulations," Proceedings of the 23rd Particle Accelerator Conference (PAC09) 4-8 May 2009, Vancouver, British Columbia, Canada, p. 2850 (available online at http://accelconf.web.cern.ch/AccelConf/PAC2009/papers/we6rfp028.pdf).

23. J. Lettry et al., *Nucl. Instr. and Meth. Phys. Res. B* **126**, p. 130 (1997).

24. S. Lukic et al., *Nucl. Instr. and Meth. Phys. Res. A* **565**, p. 784 (2006).

25. TRIUMF, Yields for Uranium Targets, http://mis.triumf.ca/science/planning/yield/target/U.